Palaeogeography, Palaeoclimatology, Palaeoecology 585 (2022) 110744

Contents lists available at ScienceDirect

Palaeogeography, Palaeoclimatology, Palaeoecology

journal homepage: www.elsevier.com/locate/palaeo

Middle Triassic to Late Jurassic climate change on the northern margin of the South China Plate: Insights from chemical weathering indices and clay mineralogy

Xianduo Dai [a], Yuansheng Du [a,*], Martin Ziegler [b], Chaowen Wang [c], Qianli Ma [a], Rong Chai [a], Hua Guo [a]

[a] State Key Laboratory of Biogeology and Environmental Geology, School of Earth Sciences, China University of Geosciences, 430074 Wuhan, China
[b] Department of Earth Sciences, Faculty of Geosciences, Utrecht University, 3584, CB, Utrecht, the Netherlands
[c] Gemological Institute, China University of Geosciences, 430074 Wuhan, China.

ARTICLE INFO

Editor: Prof. Thomas Algeo

Keywords:
Mesozoic
Zigui Basin
Dangyang Basin
Mudrock
The chemical index of alteration

ABSTRACT

The early Mesozoic greenhouse period was characterized by variable climate conditions. The driving mechanisms of this long-term variability are unclear due to a lack of full-period climate reconstructions. In particular, reconstructions of the terrestrial environment are rare, especially reconstructions representing South China during the early Mesozoic period. We focused on the major, trace and rare earth element compositions and clay mineralogy of 173 mudstones from the northern margin of the South China Plate. These data were used as proxies to evaluate the weathering intensity and reconstruct the climate variability from the Middle Triassic to the Late Jurassic after considering the potential effects of provenance, diagenesis and sedimentary sorting and recycling. From the latest part of the Triassic to the early Middle Jurassic, five well-correlated chemical weathering indices, the chemical index of alteration (CIA), chemical index of weathering (CIW), plagioclase index of alteration (PIA), sodium depletion index (τNa) and weathering index of Parker (WIP), imply an advanced degree of chemical weathering (e.g., CIA_{corr}, the corrected CIA, ranging from 71.1 to 88.0) and a clay mineral assemblage zone with abundant kaolinite. Together, these findings indicate a dominant humid climate. In the pre-Late Triassic and post-Middle Jurassic, the dominant seasonally arid climate was characterized by low and widely variable chemical weathering index values (e.g., CIA_{corr} values of 59.4–85.4) and clay mineral assemblage zones containing chlorite, smectite and mixed-layer illite–smectite but less kaolinite. We suggest that PCO_2 variations, the megamonsoon effect, plate motion and regional topography all contributed to the observed climate changes during the early Mesozoic.

1. Introduction

The Triassic and Jurassic have been conventionally viewed as periods of largely consistent greenhouse climate conditions (Hallam, 1985; Jenkyns, 1988). During these periods, atmospheric CO_2 concentrations were as high as 2000 ppm (Foster et al., 2017), and global average temperatures were 5–10 °C higher than the present-day temperatures (Berner and Kothavala, 2001; Sellwood and Valdes, 2008). No clear evidence for the presence of polar ice during the Triassic and Jurassic has been found (Holz, 2015; Ruebsam et al., 2019), and the interior of the supercontinent Pangaea was a vast evaporitic environment (Parrish et al., 1982; Hallam, 1985).

However, an increasing number of studies have revealed remarkable variabilities in the Triassic and Jurassic greenhouse climates. For example, climate simulations by Kutzbach and Gallimore (1989) revealed zonal climate heterogeneity on an interannual time scale during the Triassic, and this heterogeneity was reproduced in subsequent studies and extrapolated to other periods in the Mesozoic (Sellwood and Valdes, 2006, 2008). Long-term climate oscillations in the Triassic were characterized by multiple periods of fluctuating temperatures and rainfall as recognized from marine shell oxygen isotopes, terrestrial paleosol records and paleoflora records (Stefani et al., 2010; Retallack,

* Corresponding author.
E-mail addresses: xianduodai@cug.edu.cn (X. Dai), duyuansheng126@126.com (Y. Du), M.Ziegler@uu.nl (M. Ziegler), cwwang_cug@aliyun.com (C. Wang), maqlcug@126.com (Q. Ma), rong_chai@163.com (R. Chai), guohuacug@163.com (H. Guo).

https://doi.org/10.1016/j.palaeo.2021.110744
Received 12 June 2021; Received in revised form 27 October 2021; Accepted 27 October 2021
Available online 3 November 2021

2009a, 2009b; Retallack, 2013; Trotter et al., 2015). After the short hothouse event and mass extinction caused by the eruption of the Central Atlantic Magmatic Province (CAMP) at the Triassic–Jurassic boundary (TJB) (e.g., Foster et al., 2017; Pálfy and Smith, 2000), the Jurassic climate was generally warmer and wetter than the Triassic climate (Boucot et al., 2013; Harris et al., 2017). However, the obtained compilation of cold-climate-sensitive sediment records (Price, 1999) and shell oxygen isotope data (Dera et al., 2011; Grossman, 2012) indicate that Jurassic greenhouse conditions were interspersed with several short cold snap periods with abrupt seawater temperature decreases of 5–10 °C (Dromart et al., 2003; Sellwood and Valdes, 2008; Korte et al., 2015; Price et al., 2016; Bodin et al., 2020). As abundant previous paleoclimate studies mainly focused on the western Tethys marine realm, the evolution of the early Mesozoic terrestrial paleoclimate, particularly that in the eastern Tethys realm, has received much less attention. Although previous studies have confirmed that some highlighted short-term paleoclimate events, such as various greenhouse crisis events, the Carnian Pluvial Episode (CPE) and the Toarcian Oceanic Anoxic Event (T-OAE) (e.g., Retallack, 2009a; Sun et al., 2016; Fu et al., 2017; Xu et al., 2017; Jiang et al., 2019; Retallack and Conde, 2020), had at least an inter-Tethyan influence, the patterns and comparability of long-term paleoclimate changes between the western and eastern Tethys marine/land facies are poorly understood, partially because continuous long-term paleoclimate reconstructions from the eastern Tethys realm representing the Triassic and Jurassic in both the marine and terrestrial facies are still scarce.

Following the collision of the North China Craton and the South China Craton during the Indosinian Orogeny, a series of foreland basins (e.g., Sichuan, Zigui and Dangyang Basins) developed on the northern margin of the South China Plate and preserved complete lower Mesozoic terrestrial strata (Liu et al., 2005; Dong and Santosh, 2016). These basins provide ideal sites and materials for investigating the evolution of the early Mesozoic terrestrial paleoclimate. Previous climate reconstruction work in these basins has mainly concentrated on paleovegetation and sedimentology records (e.g., Zhang and Meng, 1987; Wang, 2002; Wang et al., 2010; Pole et al., 2018; Li et al., 2020), while successive geochemical data are lacking, limiting further modeling and intercomparisons of long-term climate change during the Triassic and Jurassic. The elemental–geochemical and detrital–clay mineralogical compositions of mud sediments document the chemical weathering conditions and therefore the paleoclimate evolution of the provenance because the advanced and weak degrees of chemical weathering of a source rock generally correspond to a warm and wet climate and a cold and/or arid climate, respectively (e.g., Singer, 1980; Nesbitt and Young, 1982; Yang et al., 2016). Here, we present geochemical and clay mineralogy data from 173 mudstone samples obtained from the Zigui and Dangyang Basins, which are two terrestrial foreland basins on the northern margin of the South China Plate, to (a) provide a unique record of the long-term weathering evolution and climate change that occurred in South China during the Middle Triassic–Late Jurassic and (b) reveal the possible driving mechanism of these changes.

2. Geological background

2.1. Tectonics

Tectonic reconstructions imply that the South China Craton was located at low to middle latitudes in the eastern Tethys Ocean during the Triassic and Jurassic (Golonka et al., 2018; Xu et al., 2017; Huang et al., 2018). The two studied basins, the Zigui and Dangyang Basins, are the eastern extensions of the paleo-Sichuan Lake and are part of the foreland basin belt that formed during the collision of the South China and North China Cratons during Indosinian tectonism (Fig. 1A, Dong and Santosh, 2016). The Zigui Basin is bounded by the Shennongjia Uplift in the north and the Enshi Arcuate Fold Belt in the south. This basin was separated from the Sichuan Basin to the west by the Qiyueshan Fault and from the Dangyang Basin to the east by the parallel Huangling anticline at a distance of approximately 80 km. The Zigui and Dangyang Basins contain well-preserved Mesozoic strata that are ideal for investigating the Triassic–Jurassic terrestrial paleoclimate.

2.2. Lithostratigraphy and age

The Xiaozhanghe section (31°23′14″ N, 110°42′57″ E; elevation: 284 m) in the Dangyang Basin and the Xuanwudong (30°54′16″ N, 110°43′01″ E; elevation: 194 m) and Xiakou sections (31°08′32″ N, 110°46′53″ E; elevation: 210 m) in the Zigui Basin were selected for this study (Fig. 1B). The studied strata are (1) the Badong Formation in the Xiaozhanghe section (Fig. 2A), (2) the Jiuligang and Tongzhuyuan formations in the Xuanwudong section (Fig. 2B), and (3) the Qianfoya, Shaximiao, Suining and Penglaizhen formations in the Xiakou section (Fig. 2C). The total thickness of the studied formations is approximately 2818 m.

The Badong Formation conformably overlies the dolomites of the Jialingjiang Formation and consists of massive red clayey mudstones (lower and upper members) and carbonates (middle member; Fig. 3A–C). Widely developed calcisol contains abundant trace fossils (Fig. 3C) in mudstone sediments. Tempestites in the carbonates (e.g., edgewise limestone and hummocky cross-bedding; Fig. 3A–B) indicate that the Badong Formation was deposited in a shallow sea and tidal flat

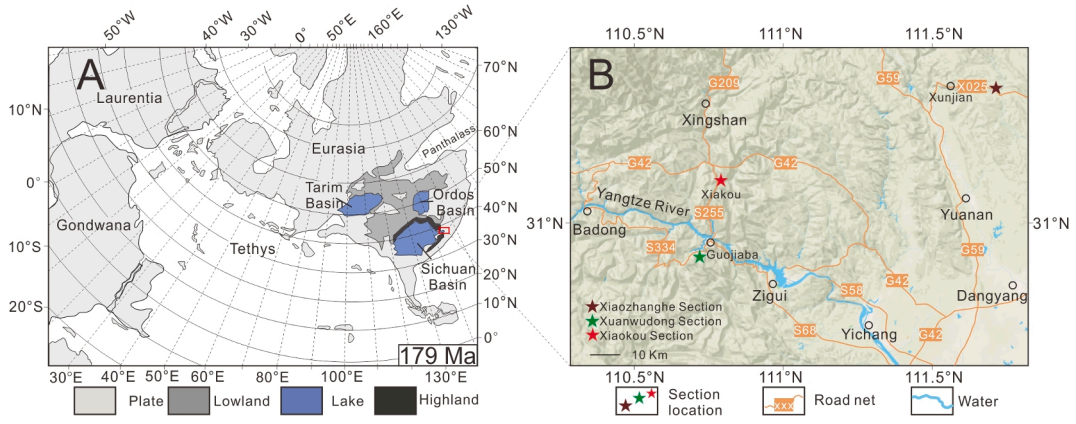

Fig. 1. Locations of the study area and sections. (A) Location of the study area (red rectangle) on an Early Jurassic paleogeography map at 179 Ma modified from Xu et al. (2017). (B) Map of the study area, showing the locations of the Xiaozhanghe section (brown star) in the Dangyang Basin and the Xuanwudong section (green star) and Xiakou section (red star) in the Zigui Basin. (For interpretation of the references to colour in this figure legend, the reader is referred to the web version of this article.)

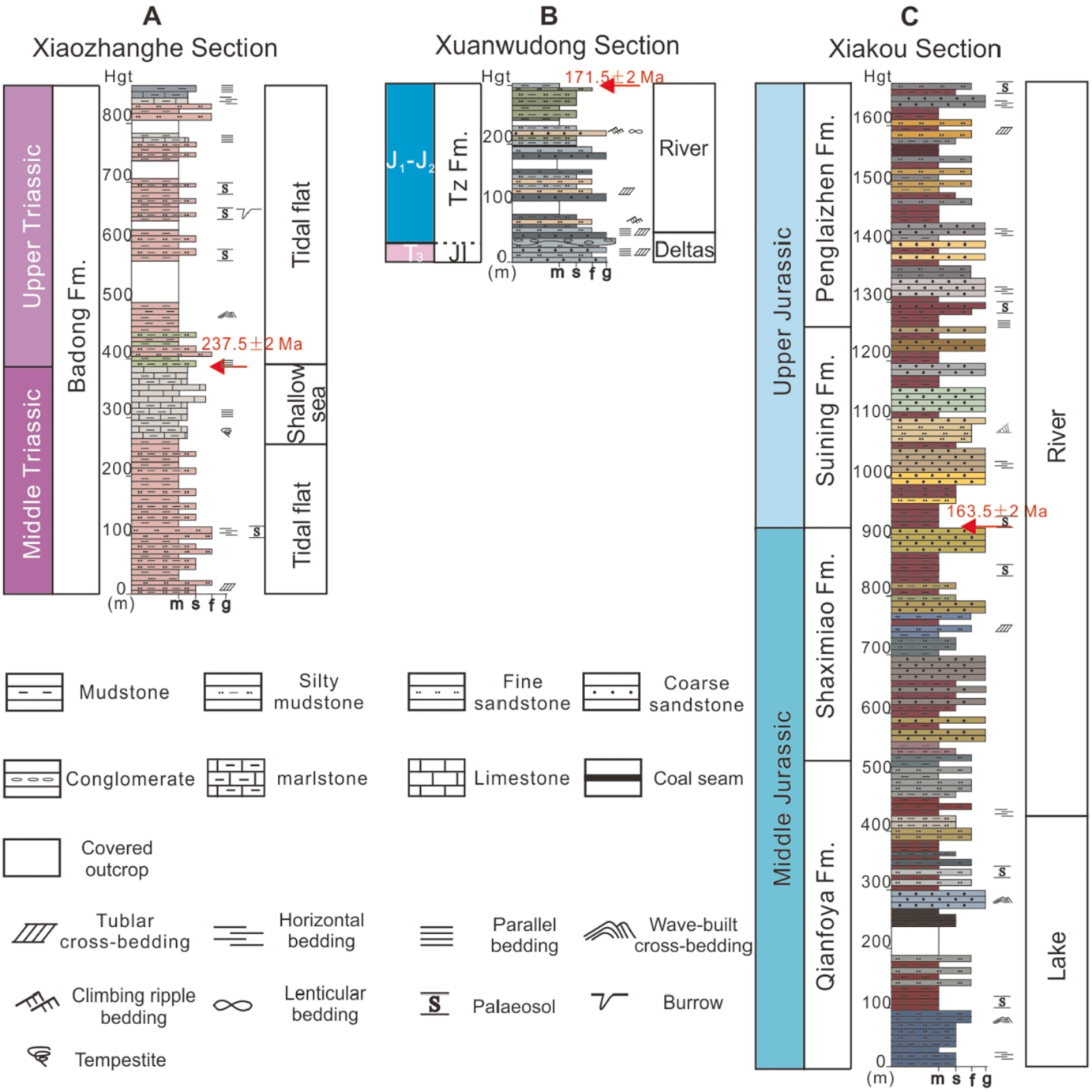

Fig. 2. Stratigraphy of the studied Middle Triassic–Upper Jurassic strata of the Badong Formation in the Xiaozhanghe section in the Dangyang Basin, the Jiuligang (Jl) and Tongzhuyuan (Tz) formations in the Xuanwudong section and the Qianfoya, Shaximiao, Suining, and Penglaizhen formations in the Xiakou section in the Zigui Basin, showing facies interpretations and the locations of zircon U–Pb dated samples (red arrows). (A) Stratigraphic column of the Xiaozhanghe section in Dangyang Basin. The tuff zircon U–Pb age of 237.5 ± 2.0 Ma is from Ma et al. (2019). (B–C) Stratigraphic columns of the Xuanwudong and Xiakou sections in the Zigui Basin, respectively. The ages of 171.5 ± 2.0 and 163.5 ± 2.0 Ma are unpublished minimum detrital zircon U–Pb dates. Abbreviations: Hgt = Stratigraphic height, JL = Jiuligang Formation, Tz Fm. = Tongzhuyuan Formation, m = mudstone, s = silty mudstone, f = fine sandstone, and g = coarse sandstone (i.e., gritstone). (For interpretation of the references to colour in this figure legend, the reader is referred to the web version of this article.)

environment influenced by intermittent high-energy events. The Jiuligang Formation conformably overlies the Badong Formation and is truncated by a 7.4-m-thick basal channel conglomerate of the Tongzhuyuan Formation in the Xuanwudong section. The Tongzhuyuan Formation consists of conglomerates and silty sandstones that are intercalated with coal seams and black shales (Fig. 3D–F). The channel deposits and bimodal cross-bedding (Fig. 3F) found in these rocks are indicative of a marine–terrigenous delta sedimentary environment that gradually regressed to a riverine environment during the Late Triassic–Early Jurassic.

The Badong Formation crops out widely in the northeastern South China Craton, including in eastern Chongqing, northwestern Hubei and northwestern Hunan Provinces. The stratigraphic age of the Badong Formation is controversial. Fossil assemblages in the Dangyang Basin have been used to infer that the entire Badong Formation is Middle Triassic in age (Zhang and Meng, 1987). However, this result is

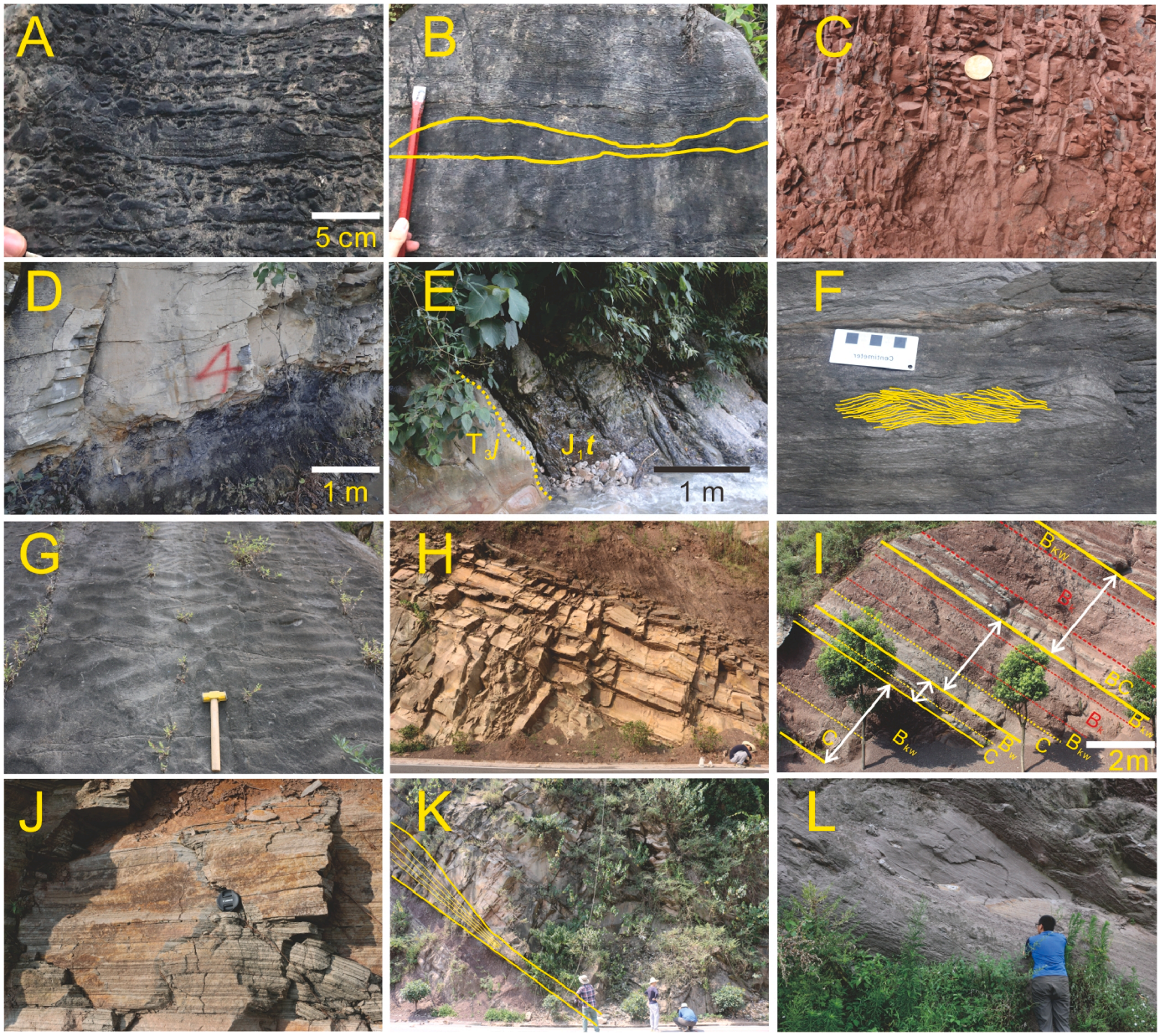

Fig. 3. Typical sedimentary features in the studied sections. (A) Edgewise limestone in the Middle Triassic Badong Formation ($T_{2-3}b$). (B) Hummocky cross-bedding in the Badong Formation ($T_{2-3}b$). (C) Supratidal facies of pedogenic mudstone with burrows in the Badong Formation ($T_{2-3}b$). (D) Coal deposits in the Jiuligang Formation (T_3j). (E) Unconformable contact between the basal conglomerate of the Tongzhuyuan Formation (J_1t) and Jiuligang Formation (T_3j). (F) Herringbone cross-bedding in the Tongzhuyuan Formation (J_1t). (G) Ripple marks in the Middle Jurassic lake-shore facies of the Qianfoya Formation (J_2q). (H) Sandy bed in the Shaximiao Formation (J_2sx) covered by floodplain-deposited pedogenic mudstone of the Suining Formation (J_3s). (I) Compound monsoonal calcisol with diffused carbonate nodule (Bk) horizon with thicknesses of up to ~1.5–2.0 m in the Suining Formation (J_3s). The white double-headed arrows and the red-dashed lines and letters mark the ranges of calcisol and thick Bk horizon, respectively. (K) Wedge-shaped cross-bedding in blocky sandstone with an erosional basal surface that rests on the mudstone of the Suining Formation (J_3s). (L) Blocky, pebbly sandstone in the Penglaizhen Formation (J_3p). (For interpretation of the references to colour in this figure legend, the reader is referred to the web version of this article.)

inconsistent with the abundant Late Triassic flora (e.g., *Equisetites arenaceus*, *Scytophyllum, Sphenozamites* and *Sinoctenis*) that can be found in the upper member of the Badong Formation in the Zigui Basin (Meng and Li, 2003). The zircon U–Pb age of 237.5 ± 2.0 Ma of a tuff in the uppermost part of the second member of the Badong Formation in the Zigui Basin (Ma et al., 2019) constrains the age of the lower and middle members to the Middle Triassic Anisian–Ladinian stages and the age of the upper member to the Late Triassic. This age marker is also applicable in the Xiaozhanghe section of the Dangyang Basin (Fig. 2A) because of the good correlation of Middle–Upper Triassic strata between the Dangyang and Zigui Basins (Meng and Li, 2003). Overlying the Badong Formation, the Jiuligang Formation (formerly known as the Shazhenxi Formation) in the Zigui Basin is correlated with the Xujiahe Formation in the adjacent Sichuan Basin, which has been assigned to the latest Norian to Rhaetian in age based on the occurrence of typical Late Triassic flora (e.g., *Shenozamites cf. changi Sze*, *Sphenozamites Marioni Counillon* and *Sphenozamites Fenshuilingensis Meng*; Meng and Li, 2003) and D–C sporopollenin assemblages (*Kyrtmiosporites*, *Zebraspories*, *Canalizonospora*, *Tigrispories*, *Annulispora*, *Trizonites*, *Aratrisporites*, *Cadargasporites*, *Dictyoph yllidites* and *Concavisporites*; Zhang and Meng, 1987), and this age also agrees with the findings of a magnetostratigraphic study (Li et al., 2018). Thus, the upper member of the Badong

Formation in the Xiaozhanghe section is roughly constrained as Carnian–Norian in age. The TJB has been placed at the unconformity between the Jiuligang and Tongzhuyuan formations in the study area (Chen et al., 2002; Meng, 2007, 2010). The Tongzhuyuan Formation in the Zigui Basin contains abundant fossil plants dominated by *Coniopteris–Czekanowski* and *Coniopteris–Ptilophyllum* assemblages, *Margaritifera (Qiyangia)* bivalve assemblages, and *Cyathidites minor* and *Classopoilis* sporopollenin assemblages, which indicate an Early Jurassic age. A minimum detrital zircon U–Pb age of 171.5 ± 2.0 Ma (Chai et al., unpublished data) from the uppermost Tongzhuyuan Formation in the Wenhua section, which is located 8 km southeast of the Xuanwudong section, indicates that the sample is Early Jurassic (Hettangian) to earliest Middle Jurassic (Aalenian) in age.

The five coarsening-upward stratigraphic units in the Xiakou section from the Qianfoya to Penglaizhen formations are terrestrial red bed deposits that conformably overlie the Tongzhuyuan Formation, which are marked at its top by a green gritstone horizon. The main sedimentary rocks are red mudstone, variably colored sandstone, siltstone and abundant paleosols. The Qianfoya Formation consists of bluish-gray siltstone at the base and an increasing amount of red mudstone in the upper section. This lithological association and the occurrence of ripple marks (Fig. 3G) indicate a lacustrine depositional environment of this unit. The Qianfoya Formation and overlying Shaximiao Formation are separated by 22-m-thick gray–green massive feldspathic quartz sandstone. The Shaximiao Formation consists of multicolored fine to coarse sandstones interbedded with siltstone–mudstone. The Qianfoya and Shaximiao formations are considered to be Middle Jurassic in age, and their ages are constrained by the sporopollenin assemblages of *Cyathidites minor–Classopollis–Callialasporites* that were widely distributed in Eurasia during the Middle Jurassic (Chen and Zhang, 2002, 2004).

The Shaximiao Formation is sequentially and conformably overlain by the Suining and Penglaizhen formations. The base of the Suining Formation is an ~120-m-thick bright red aridisol (Fig. 3H–I), and its upper part consists of thick-bedded gritstone interbedded with thin-bedded red mudstone. The boundary between the Suining and Penglaizhen formations is marked by a blocky purple–gray sandstone interbedded with a red mudstone. The amount of purple gray–yellow, fine to conglomeratic sandstone increases toward the upper part of the Penglaizhen Formation. The dual structure (Fig. 3H), floodplain paleosol deposits (Fig. 3I), river-related bedding (Fig. 3J–K), and channel facies pebbly deposits (Fig. 3L) indicate that the depositional environment of the uppermost Qianfoya to Penglaizhen Formation deposits was fluvial sedimentation.

In the Xiakou section, a minimum detrital zircon U–Pb age was obtained from a sample collected 2.5 m above the boundary between the Shaximiao and Suining formations (Fig. 3H) and yielded an age of 163.5 ± 2.0 Ma (Ma et al., unpublished data). This is consistent with the basal age of the Late Jurassic Oxfordian stage, implying a Middle Jurassic age (Aalenian–Callovian) of the Qianfoya to Shaximiao formations. The Suining and Penglaizhen formations represent the main Upper Jurassic strata, from the latest Callovian stage through the Tithonian stages (Deng et al., 2017a).

3. Samples and methods

3.1. Geochemical analysis

A total of 173 mudstone samples were collected from field outcrops. Care was taken to avoid surface contamination for the whole-rock geochemical analyses, which were conducted at Australian Laboratory Services in Chemex, Guangzhou, China. The samples were trimmed to remove visible veins and weathered surfaces and then powdered to smaller than 200 mesh. The concentrations of major elements in the samples were measured with a PANalytical PW2424 X-ray fluorescence spectrometer. The analytical accuracy was better than ±2%, and the precision was better than ±5%. The trace element abundances were measured with a Perkin–Elmer Elan 9000 inductively coupled plasma–mass spectrometer (ICP–MS) and an Agilent VISTA ICP –atomic emission spectrometer (ICP–AES). The analytical precision and accuracy were generally better than ±10%.

3.2. X-ray diffraction analysis

The clay mineral fractions (<2 μm) of 173 mudstone samples were extracted from whole-rock powder after disaggregation in an ultrasonic bath with deionized water by multiple centrifugation. Air-dried and oriented clay mineral slides were prepared by pipetting the clay fraction of each sample onto a glass slide. To identify smectite and/or mixed-layer illite–smectite (I/S), ethylene glycol-saturated clay minerals were prepared by treating the oriented air-dried samples in a container with ethylene glycol at 70 °C for 12 h. X-ray diffraction (XRD) analyses of the clay samples were performed with a PANalytical X' Pert Pro instrument using a Cu–Ni tube operated at 40 kV and 40 mA at the State Key Laboratory of Geological Processes and Mineral Resources, China University of Geosciences, Wuhan, China. The samples were scanned from 3° to 35° (2θ) at a scan rate of 2°/min and step size of 0.02° using CuKα radiation and a graphite monochromator. The software package used for the XRD analysis was XrayRun. The clay minerals were identified by their characteristic reflections using the methods of Moore and Reynolds (1989). The relative abundances of different clay minerals were estimated using the area of the glycolate basal (001) peak with the background removed (Biscaye, 1965).

3.3. Scanning electron microscopy

For scanning electron microscopy imaging, blocks of the rock samples were selected and Pt-coated. The block samples were examined with a SU8000 scanning electron microscope (SEM) at the State Key Laboratory of Biogeology and Environmental Geology, China University of Geosciences, Wuhan, China. The SEM was operated at an accelerating voltage of 25 kV and a beam current of 1–3 nA.

4. Results

4.1. Geochemical data

The main geochemical features of the samples are shown using box plots of the major elements (Fig. 4A–F; Table S1) and multielement plots of trace elements and rare earth elements (REEs). The representative elements are shown grouped into three types in Fig. 4G–H, and the data are listed in Tables S2–S3. Samples from the Jiuligang and Tongzhuyuan formations in the Xuanwudong section are characterized by high Al_2O_3 (8.66–18.41 wt.%; average = 14.95 wt.%) and low CaO, Na_2O, K_2O and FeO + MgO contents. However, samples from the Badong Formation in the Xiaozhanghe section and Qianfoya to Penglaizhen formations in the Xiakou section show opposite features. Additionally, samples from the Badong Formation have higher CaO contents (0.47–25.60 wt.%; average = 10.39 wt.%) than samples from the other formations (Fig. 4C).

The trace element contents of the samples were normalized to the South Qinling upper continental crust (Fig. 4G; Gao et al., 1998) and show distinct negative Ba and Sr anomalies enriched in high-field-strength elements, such as Th and U, and negative transition element (Ni, Cr, Co, V) anomalies. The post-Archean Australian shale (PAAS)-normalized REE patterns (Fig. 4H; Taylor and McClennan, 1985) of samples from different strata show similar trends.

4.2. Clay mineralogy

The XRD patterns and SEM images of representative samples are shown in Fig. 5, and the clay mineral relative contents of all samples are listed in Table S4. Illite (10, 5, 4.5, and 3.33 Å) is ubiquitous in the three

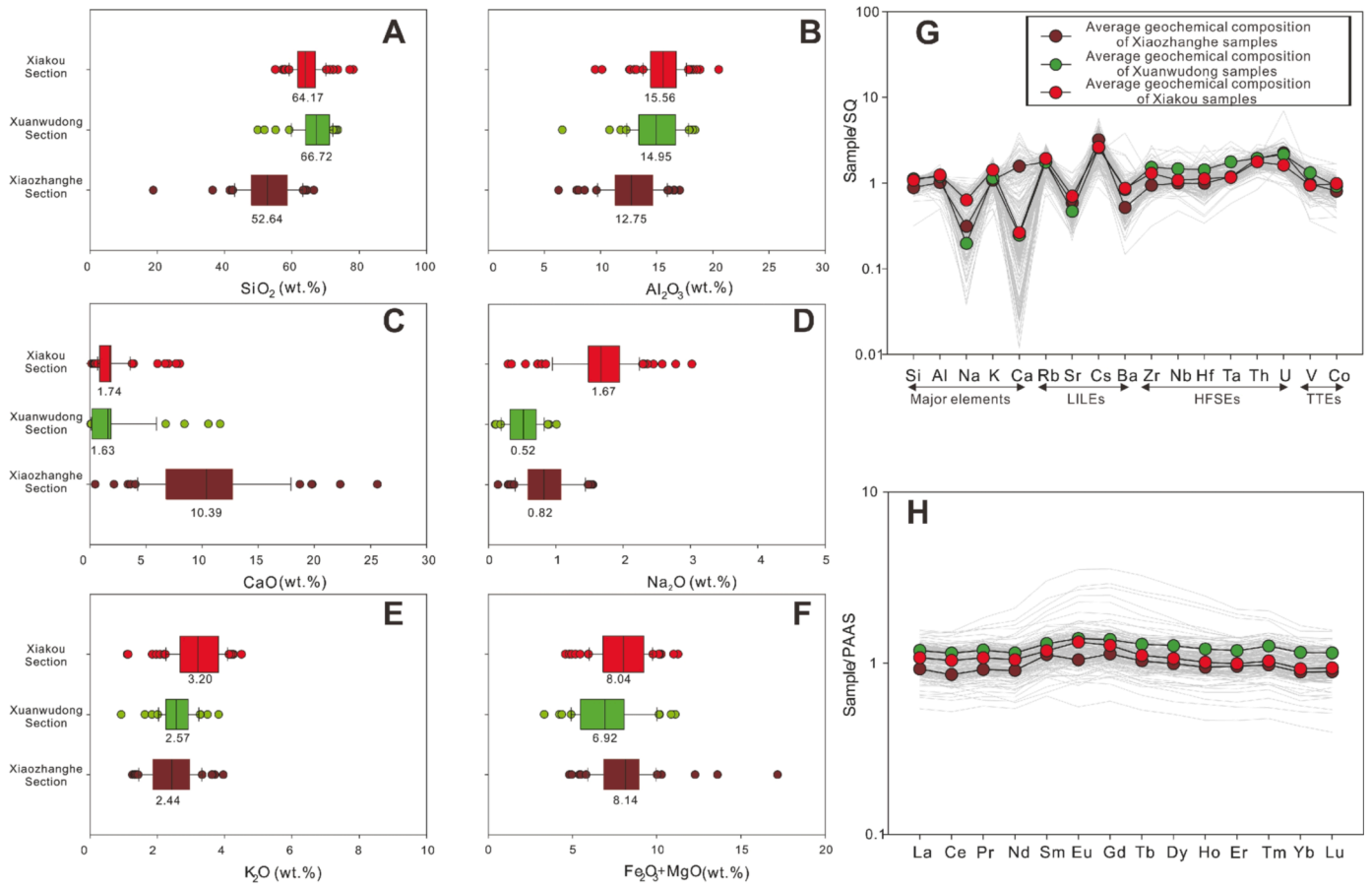

Fig. 4. Plots of major and trace elements in the 173 mudstone samples from the Xiaozhanghe, Xuanwudong, and Xiakou sections. (A–F) Box plots of major element contents. The black lines and values in the colored boxes are the average major element contents. (G) Southern Qinling upper crust (SQ)-normalized major and trace element diagrams and (H) Post-Archean Australian Shale (PAAS)-normalized REE patterns of all mudstone samples (gray dashed lines). The three colored solid lines are the average compositions of the samples from the three studied sections. The SQ values are from Gao et al. (1998), and the PAAS values are from Taylor and McClennan (1985).

sections (16.5–97.5 wt.%). Except for samples XKB-25, XKB-31 and XKB-54, all samples contain chlorite (0.03–62.3 wt.%), which is negatively correlated with the presentation of kaolinite (7.1 and 3.57 Å). Kaolinite occurs mainly in the Tongzhuyuan Formation and at the bottom of the Qianfoya Formation (maximum of 47.9 wt.%; Fig. 5). Mixed-layer I/S (broad 10–14 Å reflection, which is expandable after glycolate treatment) and smectite (~17 Å) (Fig. 5) are present in high contents in the Xiakou Section, with maximum contents of 54.3 and 53.6 wt.%, respectively. Most of the clay minerals have flaky or platy shapes with irregular, ragged and embayed outlines suggesting that the clay is primarily of detrital origin and experienced chemical weathering in its source region.

5. Geochemical climate proxies

5.1. Chemical weathering indices

Various chemical weathering indices defined by the ratios between the concentrations of mobile and immobile elements in sediments can be used to trace chemical weathering and past climate patterns. The CIA was proposed by Nesbitt and Young (1982) in a study of the early Proterozoic glacial–interglacial climate and has been broadly applied to different regions and strata of various ages (Wang et al., 2020), including strata from the Mesozoic (e.g., Jian et al., 2013; Nordt et al., 2015; Casacci et al., 2016). We used the CIA, CIW (Harnois, 1988), PIA (Fedo et al., 1995), τNa (Rasmussen et al., 2011), and WIP (Parker, 1970) to examine the potential effects of sedimentary processes and lithology and to reconstruct the paleoclimate. These indices are defined in Table S5.

5.2. Climate index values and Sr/Cu ratios

Climate index values (C-value; Zhao et al., 2007, Table S5) and Sr/Cu ratios (Lerman, 1978) have been used to reconstruct the Mesozoic paleoclimate in the Ordos and Qaidam Basins (Cao et al., 2012; Qiu et al., 2015). The underlying concepts of these two proxies are as follows: under humid conditions, Fe, Mn, Cr, Ni, V and Co flocculated and precipitated in the sediments in colloidal form, leading to increased C-values, while larger-ionic radii alkali metals (Ca, Mg, K, Na, Sr, and Ba) precipitated in arid climates in the form of salts, leading to decreased C-values. A Sr/Cu ratio of >5 implies a hot and arid climate, but Sr/Cu <5 indicates a humid climate.

6. Discussion

6.1. Provenance interpretation of samples in the Zigui and Dangyang Basins

Sediment compositions can reflect the chemical weathering of the corresponding source rocks (McLennan, 1993). In addition, the composition of a source lithology is a key factor in its in situ chemical weathering and the transport and deposition of the resulting sediment in a basin (Kamei et al., 2012). Therefore, provenance stability is crucial when forming climate interpretations from chemical weathering

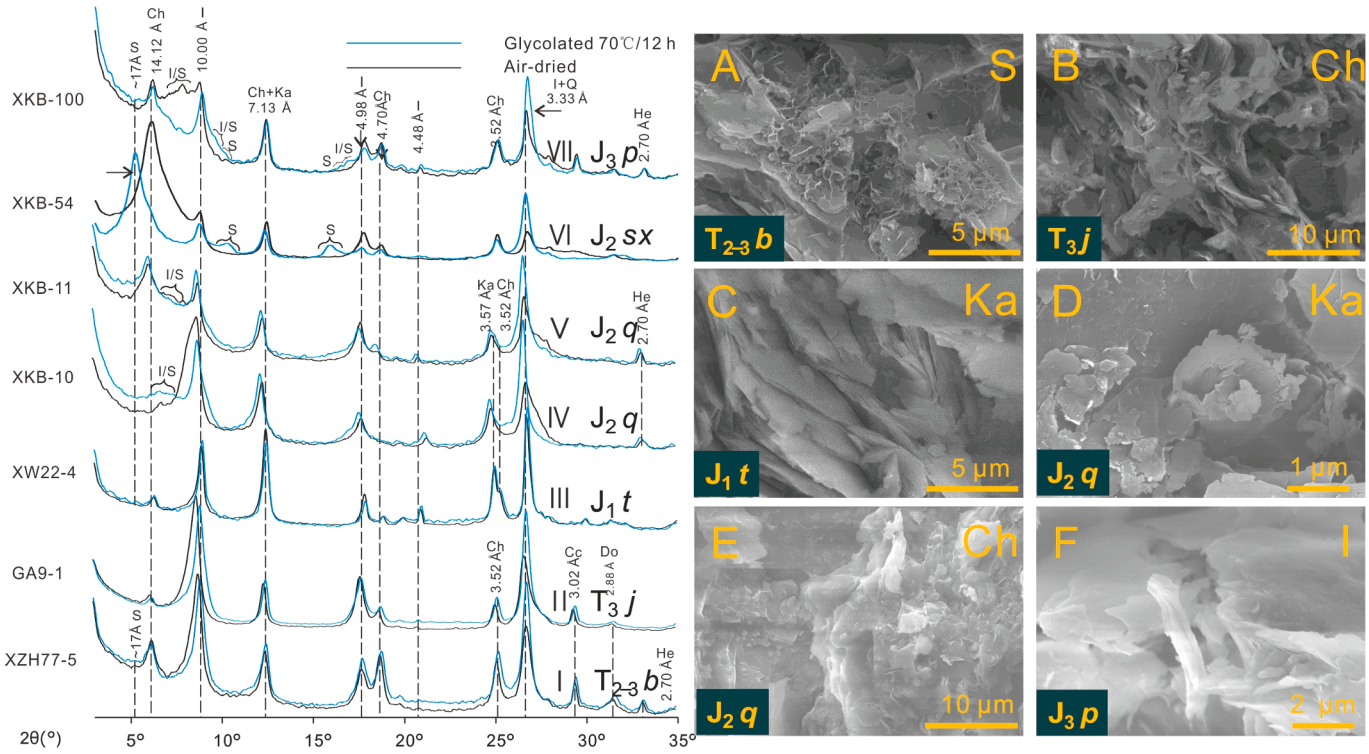

Fig. 5. (I–IV) Air-dried and ethylene-glycolated X-ray diffraction (XRD) patterns of the <2 μm clay fractions and (A–F) scanning electron images of representative samples. (I–II) Chlorite and illite in samples from the Badong Formation ($T_{2-3}b$) and Jiuligang Formation (T_3j). (III–IV) The appearance of kaolinite is implied by the 3.57 and 3.52 Å double peaks in the XRD patterns of the samples from the Tongzhuyuan (J_1t) and Qianfoya formations (J_2q), which have CIA values of 82.2 and 81.0, respectively. (V) Sample XKB-11 has a stronger 14.1 Å peak intensity than sample XKB-10, implying a higher chlorite content, accompanied by decreased CIA values from 81.0 to 69.9. (VI) This sample contains smectite characterized by a 17 Å peak in the glycolated pattern (Shaximiao Formation; J_2sx). (VII) Compared with the air-dried pattern, the disappearance of the broad 10–14 Å reflection and enhancement of the 17 Å peak in the glycolated pattern imply the presence of mixed-layer I/S clay minerals in sample XKB–100 (Penglaizhen Formation; J_3p). (A) Mixed-layer I/S overgrowths on other minerals in sample XZH3–1 from the bottom of the Badong Formation ($T_{2-3}b$). (B) Platy chlorite infilling intergranular pores in sample GA9–1 from the Jiuligang Formation (T_3j). (C) Laminated kaolinite in sample XW22–4 from the bottom of the Tongzhuyuan Formation (J_1t), which has a high CIA_{corr} value of 82.2. (D) Platy kaolinite with ragged and embayed edges in sample XKB-10 from the Qianfoya Formation (J_2q), indicating chemical weathering-induced dissolution. (E) Scaly chlorite in sample XKB-14 with a CIA value of 66.6. (F) Rod-shaped illite in sample XKB-106 from the upper Penglaizhen Formation (J_3p). Abbreviations: I = illite, Ch = chlorite, S = smectite, I/S = mixed-layer illite/smectite, and Ka = kaolinite.

indices. The Al_2O_3–CaO* + Na_2O–K_2O (A–CN–K) ternary diagram (Fig. 6A) is used to examine the geochemical compositions and weathering degrees of source rocks and to analyze sediment diagenesis. This plot is also a graphical representation of CIA values (Fedo et al., 1995). The studied samples that underwent a weak to moderate degree of weathering (CIA < 81.0) define a trend subparallel to the A–CN boundary in the A–CN–K diagram. This trend also deviates to the K-apex and implies a metasomatic effect of K on the samples. Other samples, mainly from the Xuanwudong section, experienced a high degree of weathering (CIA > 81.0) and trended toward the A apex along the A–K boundary. The trend of these samples extends close to the composition of the South Qinling upper continental crust (Gao et al., 1998), indicating that these samples were derived from a uniform source area with a geochemical composition similar to that of the South Qinling upper continental crust (Nesbitt and Young, 1984). Although complete REE data of the South Qinling upper continental crust are not available, the similar averaged PAAS-normalized REE patterns of samples from the three sections indicate that all of these samples had similar source materials (Fig. 4H). This apparent provenance stability is also supported by the plot of the proportion of trivalent cations ($R^{3+}/R^{3+}+R^{2+}+M^{+}$) versus the Si accumulation index (Δ4Si%). This plot highlights the predicted weathering trends of different source rock types (Meunier et al., 2013) (Fig. 6C) and shows that the studied samples were derived from chemical weathering of South Qinling upper continental crustal source rocks, which are mainly felsic rocks. An association between the uplift of the South Qinling Orogen and the massive clastic sedimentation that filled foreland basins in the Late–Middle Triassic to the Cretaceous has been demonstrated based on detrital zircon U–Pb age data, isotope geochemistry, detrital sandstone mineralogy, and paleocurrent directions (Liu et al., 2005; Chai et al., 2016; Hagen et al., 2018).

6.2. *Influence of postdepositional diagenetic alteration on samples*

The potential effects of postdepositional diagenetic alteration on the samples need to be evaluated because this type of alteration can change the primary geochemical compositions of sediments and lead to incorrect interpretations of chemical weathering indices. The weathering trends of plutonic and volcanic rocks should be parallel to the A–CN boundary in the A–CN–K diagram based on thermodynamic and kinetic calculations (Nesbitt and Young, 1984). However, the studied samples do not perfectly match the trend of South Qinling upper continental crust weathering and actually deviate slightly toward the K apex, which is indicative of K metasomatism (Fig. 6A). This metasomatism enriched the samples in K_2O and lowered the CIA values due to illitization during a postdepositional diagenetic reaction between the K-enriched pore water and clay minerals in the sediments (Fedo et al., 1995). Thus, K-correcting the CIA values (CIA_{corr}) was necessary, which was undertaken based on the method described by Panahi et al. (2000) (Table S5). The CIA_{corr} value of each sample is generally higher than the corresponding CIA value (Table S6). To evaluate the robustness of the correction, the CIW and PIA values were calculated to check the CIA_{corr} values because the former two indices are unaffected by K_2O contents and K

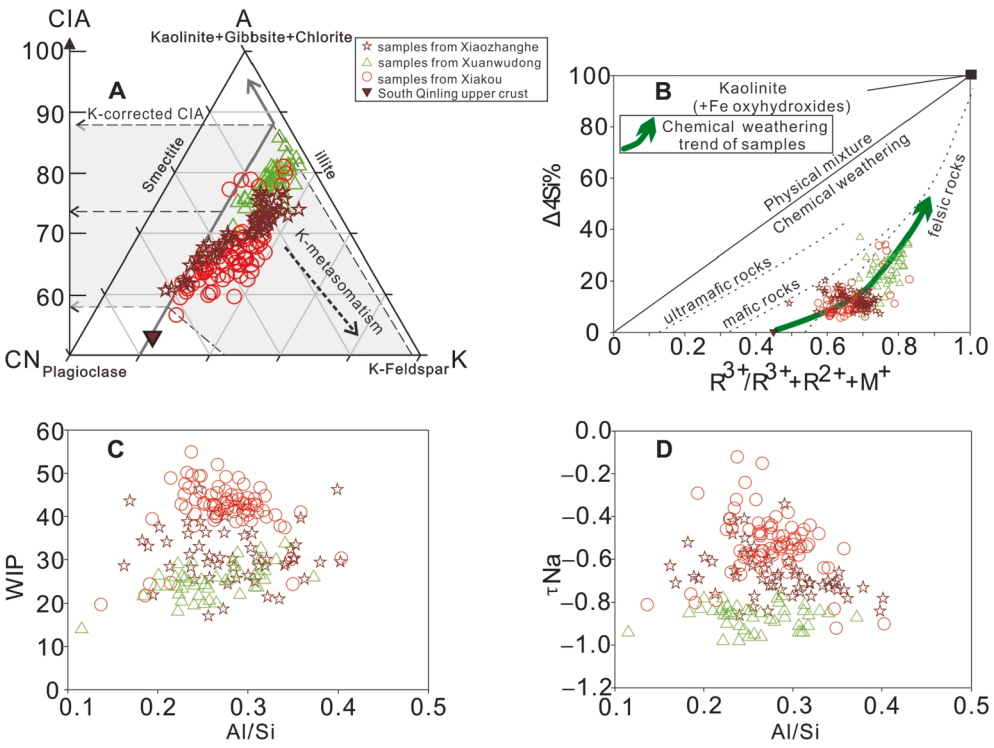

Fig. 6. (A) A–CN–K (Al_2O_3–CaO* + Na_2O–K_2O) ternary diagram (Fedo et al., 1995) showing the South Qinling upper crustal (SQ) origin of the sediments and the effects of K metasomatism. (B) Plot of the proportions of trivalent cations ($R^{3+}/R^{3+}+R^{2+}+M^{+}$) versus the Si accumulation index (Δ4Si%) (Meunier et al., 2013), showing the chemical weathering trend of the SQ upper crust (Gao et al., 1998). Plots of the Al/Si molar ratio (i.e., grain size and hydraulic sorting proxy) versus the (C) weathering index of Parker (WIP) and (D) sodium chemical depletion index (τNa). The equations used to obtain the CIA, proportion of trivalent cations, Si accumulation index, WIP, and τNa are listed in Table S4.

metasomatism. Good correlations were observed between CIA_{corr} and CIW ($r^2 = 1$; $P < 0.0001$) and between CIA_{corr} and PIA ($r^2 = 0.99$; $P < 0.0001$), implying that the effects of K metasomatism were eliminated by K-correction. Extensive K metasomatism of some samples may also hinder the use of clay mineralogy data in paleoclimate reconstructions. However, compared to the more deeply buried strata of the Xuanwudong section, the lower kaolinite and smectite contents in the more shallowly buried strata of the Xiakou Section and the original detrital morphology of the clay minerals in most samples (Fig. 5A–F) imply that postdepositional diagenetic modification was insignificant (Chamley, 1980). Although potential postdepositional cementation is implied by the unusually high CaO contents (average = 10.39 wt.%) of most samples in the Badong Formation, there is no correlation between the CaO contents and CIA_{corr} values, indicating that diagenesis had no effect on CIA_{corr} values after Ca correction based on the method of McLennan (1993) (Table S5).

6.3. Influence of sedimentary recycling and sorting effects on samples

Sedimentary sorting is caused by hydraulic effects on minerals and can modify the geochemical composition of sediments; in turn, these modified compositions can affect chemical weathering indices. For example, finer-grained sediments have higher CIA values than coarser-grained sediments, even if they have the same source (and weathering conditions) (Jian et al., 2013). To minimize the sorting effect, all samples were collected from mudstone layers. In addition, a negative correlation between the Al/Si ratios and grain sizes can be used as an indicator of hydraulic sorting (Bouchez et al., 2011) because the Al contents reflects the fine clay fraction of a rock. while the Si content reflects the coarser fraction (i.e., feldspar and quartz). Similarly, the WIP and τNa are two weathering indices negatively correlated with the sorting effect, as they are calculated based on sorting-sensitive elements, such as alkali metals and Zr. Increasing coarse fractions tend to decrease the values of both indices (Garzanti et al., 2013). However, there was no obvious correlation between the Al/Si ratio and either the WIP or τNa in this study (Fig. 6C–D), implying that sedimentary sorting is not the main factor responsible for fluctuations in the weathering index values. This is also supported by the fact that the finer-grained samples from the tidal flat facies of the Badong Formation have overall lower chemical weathering degrees than coarser-grained samples from the delta facies of the Jiuligang and Tongzhuyuan formations (Fig. 7).

Sedimentary recycling integrates the effects of syndepositional weathering with earlier weathering and diagenetic stages and can erroneously suggest that sediments have experienced extensive source weathering (Garzanti et al., 2013; Yang et al., 2016). In the Zigui and Dangyang Basins, the Middle Triassic–Upper Jurassic clastic tidal flat to terrestrial lacustrine–fluvial sequences overlie the Upper Paleozoic and Lower Triassic marine carbonates and dolomites (Wang et al., 1985); thus, it is unlikely that the underlying strata were a significant source of recycled siliciclastic materials in the studied basins. The correlation between the CIA and WIP values ($R^2 = 0.62$; $P < 0.0001$; Fig. 7) also indicates that the first-cycle sediments (Garzanti et al., 2013) were probably derived from South Qinling metamorphic and plutonic rocks.

6.4. Paleoclimate controls on source chemical weathering intensity during the Middle Triassic–Late Jurassic

The five weathering indices reveal a three-stage history of chemical weathering in the source area: (1) Middle Triassic–early Late Triassic variable weathering; (2) latest Triassic–early Middle Jurassic enhanced weathering; and (3) Middle–Late Jurassic weak weathering (Fig. 7A). Chemical weathering can reflect climatic factors such as water availability and mean annual temperature (Rasmussen et al., 2011), and the physical weathering intensity is related to tectonically driven processes and landscape morphology. This is because active physical weathering can interrupt the in situ chemical weathering processes of source rocks (Yang et al., 2016). The Qinling–Dabie Orogen in the study area was not significantly active until the main period of Indosinian tectonism during the Late Triassic–Early Jurassic (Fig. 3E; Dong and Santosh, 2016). However, compared with the relatively tectonically quiescent stages in the Middle Triassic and post-Early Jurassic, stronger chemical weathering was recorded by various weathering indices during Indosinian tectonism, implying that the climate, rather than tectonism, controlled the chemical weathering record.

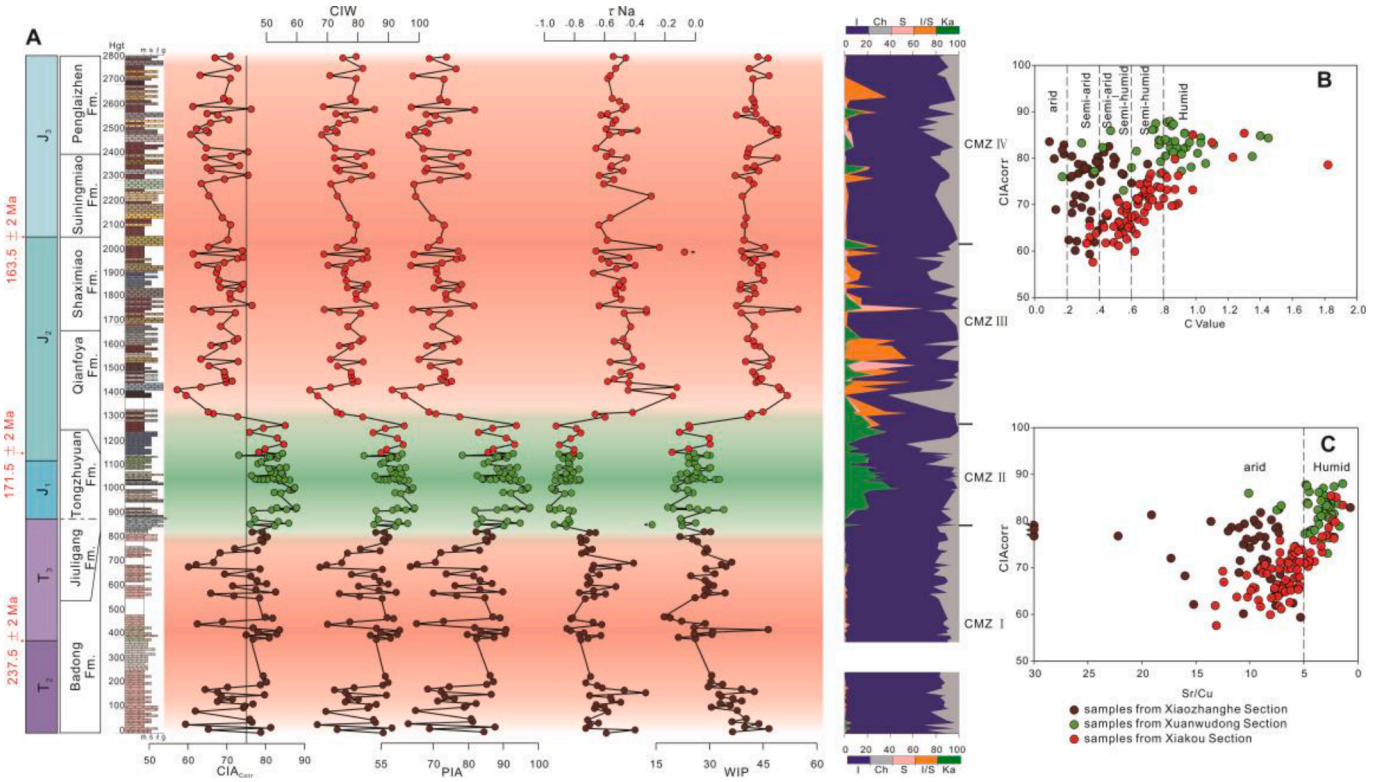

Fig. 7. Stratigraphic variations in the various weathering indices and clay mineralogy and two paleoclimate discrimination diagrams. (A) Stratigraphic variations in the corrected chemical index of alteration (CIA_{corr}), chemical index of weathering (CIW), plagioclase index of alteration (PIA), sodium chemical depletion index (τNa), weathering index of Parker (WIP), and clay mineralogy in mudstones from the three studied sections. Plots of the (B) climate index (C-value) versus CIA_{corr} and (C) Sr/Cu versus CIA_{corr} are shown. The distinguishing criteria of (B) and (C) are based on Zhao et al. (2007) and Lerman (1978), respectively. Abbreviations: I = illite, Ch = chlorite, S = smectite, I/S = mixed-layer illite/smectite, Ka = kaolinite, and CMZ = clay mineral assemblage zone. The equations used to obtain the CIA_{corr}, CIW, PIA, τNa, WIP and C-values are listed in Table S4.

6.4.1. Middle Triassic–early Late Triassic paleoclimate

Although the hot Early Triassic climate cooled during the Middle Triassic (Sun et al., 2012; Li et al., 2018), arid conditions existed across most low- to mid-latitude regions, including South China, as evidenced by the widespread evaporites, rare coal deposits and kaolinite formed during this time (Boucot et al., 2013). A general circulation model (GCM) showed that after the Late Triassic, an arid paleoclimate was still widespread in low- to mid-latitude areas in the interior of Pangaea (Sellwood and Valdes, 2006). However, abundant marine and terrestrial evidence, including conodont oxygen isotope (Trotter et al., 2015), paleosol climatology (Prochnow et al., 2006; Retallack, 2009a; Retallack, 2013) and paleobotany (Stefani et al., 2010) data, indicates that several enigmatic warm and wet episodes intermittently interrupted the arid paleoclimate in Europe and North America during the Triassic, particularly during the Late Triassic, and one such event was the CPE (Ruffell et al., 2016). The Late Triassic climate of low-latitude South China is considered to have been consistently wet due to the occurrence of hygrophilous flora (Wang et al., 2010), extensive coal deposits (Boucot et al., 2013), and alfisols (Retallack, 2009b). However, an increasing number of paleobotanical and palynological studies in the Sichuan Basin have revealed that this warm and wet environment in South China was interrupted by several dry or even cool events (Li et al., 2020; Tian et al., 2016).

The Badong Formation samples have CIA_{corr} values of 59.4–82.9, with an average of 74.13, reflecting weak to moderate chemical weathering intensities and indicating that the unstable Middle to Late Triassic arid climate of South China was frequently interrupted by humid events. Alternating wet and dry conditions are also revealed by the climatic indices, which mostly indicate semiarid to semihumid conditions (Fig. 7B–C). The C-values of the Badong Formation vary from 0.07–0.79, with an average value of 0.34, and most of the values indicate semiarid–semihumid to arid climate conditions. The Sr/Cu ratios reveal similar climate conditions. The 2.70 Å peak in the XRD spectra of the Badong Formation samples (Fig. 5I) implies the presence of hematite, which indicates an arid climate that caused the formation of Triassic red beds in the study area. In addition, the clay mineral assemblage zones (CMZs) formed during this period consist of illite and chlorite (CMZ I; Fig. 7; Table S4), and mixed-layer I/S was also identified in SEM images (Fig. 5A), suggesting a seasonal paleoclimate.

6.4.2. Latest Triassic–Early Jurassic paleoclimate

The initial breakup of Pangaea along with the eruption of the CAMP formed an embryonic mid-latitude humid belt in the Northern Hemisphere (Harris et al., 2017) and led to an abrupt increase in atmospheric CO_2 concentrations of up to 2000 ppm (Foster et al., 2017) near the TJB. Stomata-based CO_2 reconstructions from the United Kingdom and South China (Steinthorsdottir et al., 2011; Zhou et al., 2020) have shown that pCO_2 rapidly decreased to ~1000 ppm during the Hettangian, indicating short-lived hothouse conditions at the TJB. The Early Jurassic was characterized by warm and wet conditions, especially from the late Sinemurian stage to the early Pliensbachian and Toarcian stages (Gomez et al., 2016; Robinson et al., 2017), except during the cool late Pliensbachian stage (Dera et al., 2011; Tramoy et al., 2016; Kenny, 2017; Alberti et al., 2019), which was interrupted by the Toarcian warming event due to the Toarcian ocean anoxia event (Ruebsam et al., 2019). Deng et al. (2017a) reviewed the Jurassic paleoclimate evolution of China and found that the northern margin of the South China Plate, including the Zigui and Dangyang Basins, was classified as a tropical–subtropical humid climate zone during the Hettangian–Pliensbachian stages and a semiarid–semihumid climate zone during the

Toarcian stage.

The C-values of the uppermost Triassic Jiuligang Formation and Lower Jurassic Tongzhuyuan Formation samples vary from 0.17–1.54, with an average value of 0.85 (Fig. 7). Five Jiuligang Formation samples indicate arid–semiarid conditions, similar to the samples from the Badong Formation, and most Tongzhuyuan Formation samples indicate humid conditions. This reveals that progressive humidification occurred in the study area from the end of the Triassic and that this humidification peaked during the Early Jurassic. Although kaolinite is absent in the Jiuligang Formation, the CIA_{corr} values increase steadily from the top of the Badong Formation to the Jiuligang Formation and finally stabilize at high values in the Tongzhuyuan Formation, in which the extensive occurrence of kaolinite implies that the humid climate stimulated intense chemical weathering from the latest Triassic to Early Jurassic (Figs. 5 III and 7). This increase in humidity is also consistent with the hygrophyte assemblages and wide development of coal-bearing terrestrial strata in the study area and adjacent Sichuan Basin (Fig. 3D; Zhang and Meng, 1987; Meng et al., 1995; Meng and Li, 2003; Wang et al., 2010; Li et al., 2020; Tian et al., 2016).

6.4.3. Middle–Late Jurassic paleoclimate

High atmospheric CO_2 levels (1000 ppm; Foster et al., 2017), warmer northern–southern high-latitude sea surface temperatures than those measured at the present-day equator (Lécuyer et al., 2003; Jenkyns et al., 2012), and a low latitudinal global climate gradient (Sellwood and Valdes, 2008; Boucot et al., 2013) indicate that an arid and warm climate existed through the Middle–Late Jurassic. However, a compilation of $\delta^{18}O$ data has shown that the Middle Jurassic was characterized by the heaviest $\delta^{18}O$ values and several abrupt positive excursions (Dera et al., 2011). Cold-climate-sensitive sediments from the Middle Jurassic (Price, 1999) are relatively abundant compared with Mesozoic sediments and, along with the overall decrease in pCO_2, imply long-term climate cooling and drying. In both South and North China, Lower Jurassic coal-bearing strata transitioned into continental red beds (Boucot et al., 2013; Yi et al., 2019) with xerophyte assemblages (Deng et al., 2017b; Hu et al., 2017), and this transition clearly records Middle–Late Jurassic aridification.

At the bottom of the Xiakou section in the Zigui Basin, the CIA_{corr} values decrease abruptly from 85.4–57.6 and then remain low (mean $CIA_{corr} = 68.9$). For the seven samples from the bottom of the Qianfoya Formation beneath the horizon that weaken due to chemical weathering, the C-values and Sr/Cu ratios plot in the humid field in the paleoclimate discrimination diagram and then move into the arid field in which the CIA_{corr} values decrease and the CMZ transitions from II (kaolinite-rich) to III (mixed-layer I/S). This indicates that the wet Early–early Middle Jurassic climate became drier with dry–wet seasons. The CMZ changed from III to IV (smectite + illite + chlorite) in the Shaximiao Formation during the late Middle Jurassic, implying intensifying drought and a hotter climate, although the chemical weathering intensity was low and variable. Aridification of the study area after the Middle Jurassic can also be inferred from the increasing red beds above the bottom of the Qianfoya Formation (Fig. 2C), as these beds commonly contain thick aridisols (Fig. 6H–I). Sporopollenin assemblages in the Zigui Basin change from the early Middle Jurassic tropical humid ferns *Thaumatopteris* and *Phlebopteris* to late Middle Jurassic xerophyte assemblages characterized by high contents of *Classopollis* (Lin and Shang, 1980; Meng, 1999) and thermophilic bivalve assemblages of *Qiyangia–Pseudocardinia* and *Eolamprotula–Cuneopsis–Psilunio* (Zhang and Meng, 1987).

6.5. Possible driving mechanisms of paleoclimate variations

6.5.1. Atmospheric PCO_2 variations

Variation in representative greenhouse gas concentration and atmospheric PCO_2 may have controlled long-term climate and chemical weathering intensity changes in the study region during the early Mesozoic because they exert fundamental control on elements of the global climatic system, including temperature and precipitation patterns (Manabe and Wetherald, 1980; Foster et al., 2017). In general, an increase in atmospheric PCO_2 enhances the continental silicate chemical weathering process and indicates a warm and humid climate (e.g., Royer, 2014).

The Middle Triassic to Late Jurassic was a greenhouse period on Earth, with a PCO_2 at least approximately twice, on average, and up to four times preindustrial levels (approximately 500–1000 ppm). Multiproxy estimates display a 'double peak' pattern of Triassic and Jurassic CO_2 on the tectonic time scale, with elevated PCO_2 (above 2500 ppm) during the early Late Triassic and across the TJB (Fig. 8A). The increase in atmospheric PCO_2 continued from the late Middle Triassic to the first peak in the late Carnian. Atmospheric PCO_2 subsequently fell slowly to a saddle point (~1500 ppm) by the late Norian and rebounded to a second peak around TJB due to immense volcanic CO_2 outgassing from CAMP eruptions (e.g., Foster et al., 2017; Pálfy and Smith, 2000).

Based on the rough age restrictions of the study strata, the long-term variation trend of chemical weathering records (e.g., values of CIA_{corr}) in this study is in broad conformity with the 'double peak' pattern of atmospheric PCO_2 changes during the Triassic period (red arrows in Fig. 8A, B). The CIA_{corr} values of samples in the lower part of the Xiaozhanghe section, which includes the Middle Triassic strata, gradually increase to a peak value of 83.5 (XZH 62–1) at the bottom of the Upper Triassic. Then, the CIA_{corr} curve decreases to a saddle point of 60.1 (XZH 77–2) in the middle Upper Triassic and subsequently rises steadily to its greatest value for all samples in the Xuanwudong section, which occurs in the Lower Jurassic. The synchronicity agrees with the potential enhancing effect of high PCO_2 and a concomitant hot humid climate on the chemical weathering intensity in the region and was also reported in other regions during the Late Triassic and Early Jurassic (e.g., Perri, 2018; Taheri et al., 2018). Except for the above PCO_2 and chemical weathering intensity variations over multimillion-year time scales, it is worth noting the strong volatility of chemical weathering records in this study on shorter timescales, which seems linked to numerous well-dated transient warm-wet greenhouse spikes associated with the western Tethys Ocean and North America during the early Mesozoic, which has also been attributed to volcanic outgassing activity (Retallack, 2009a , 2009b; Retallack and Conde, 2020; Trotter et al., 2015); however, these correlations require further investigation based on more detailed chronostratigraphic work in the studied section.

However, variations in chemical weathering intensity in the study region become decoupled with PCO_2 changes above the TJB (gray arrow in Fig. 8A, B). CAMP basaltic eruptions triggered catastrophic biotic turnover and climate shock, as indicated by high volcanic greenhouse gases, i.e., ~80,000–90,000 Gt C as CO_2 and ~ 5000 Gt C as CH_4 (Beerling and Berner, 2002) and stomatal index data suggested 3–4 °C warming during the TJB interval (McElwain et al., 1999). The eruptions played a key role in the transition from the dominant warm, semiarid–arid climate of the Triassic to the hot and humid climate of the Jurassic (Kidder and Worsley, 2010; Holz, 2015) and accounted for the humid climate and intense chemical weathering effect in the study region during the Early Jurassic. After the Triassic–Jurassic transition, the extremely high PCO_2 near the TJB quickly decreased to ~1000 ppm during the Hettangian and Sinemurian in the Early Jurassic, but the CIA_{corr} values of most samples from the Xuanwudong section remained high during the whole Early Jurassic, suggesting unabated chemical weathering until the early Middle Jurassic, when the CIA_{corr} values gradually dropped from 81.0 (XKB-10) to 56.6 (DA27-1). This remarkable weakening of chemical weathering was not driven by PCO_2 change, which shows prolonged flat values after the Early Jurassic without any dramatic drops throughout the rest of the Jurassic. More importantly, variations in PCO_2 during the early Mesozoic were unlikely to be chiefly responsible for the abovementioned strikingly low CIA_{corr} values obtained in this study, which are lower than 60. Such a weak chemical weathering effect usually corresponds to a glacial environment (e.g.,

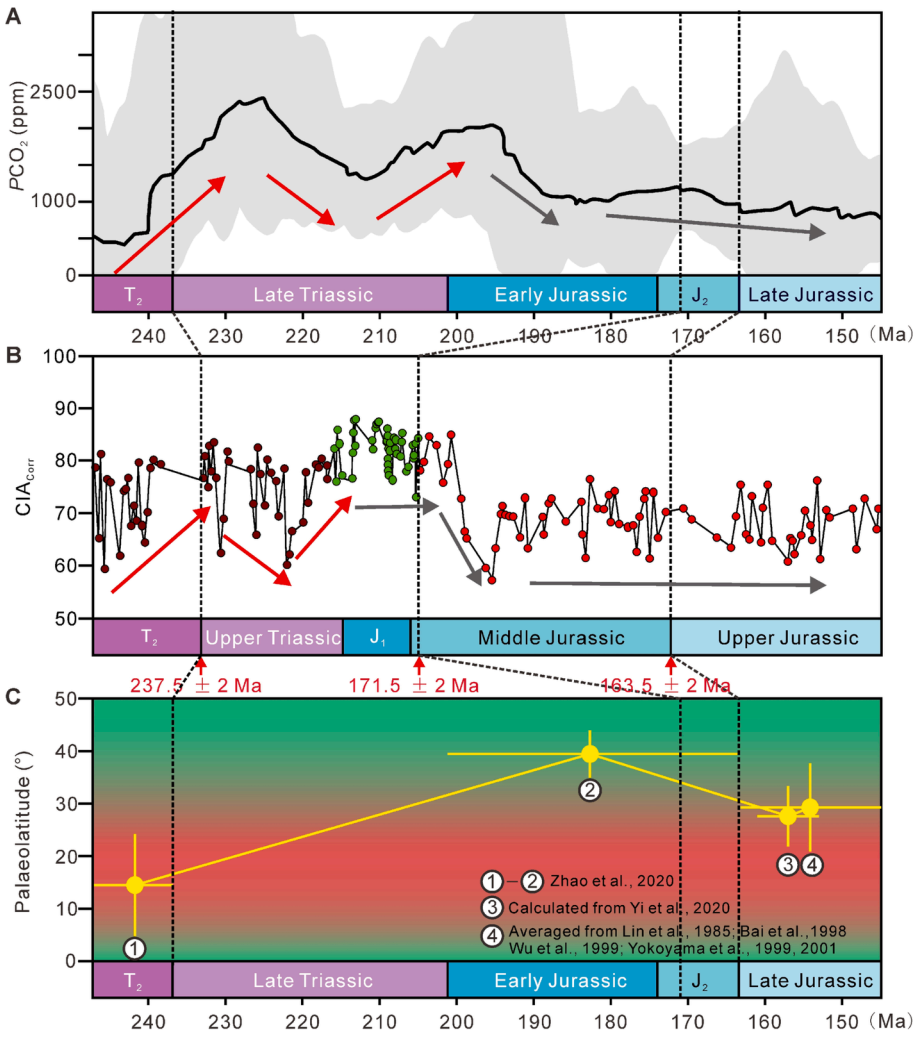

Fig. 8. Correlations of the global atmospheric changes, variations in terrestrial weathering records and shifts in paleolatitude of the South China Craton from the Middle Triassic to Late Jurassic. (A) Multiproxy-based atmospheric CO_2 concentration (black line) with minimum and maximum estimated uncertainties (gray shadow), as drawn following Gernon et al. (2021). (B) Variations in the corrected chemical index of alteration (CIA_{corr}) records from this study on the northern margin of the South China Plate. The meanings of data points in different colors are consistent with those in Fig. 7. (C) Archive of the paleolatitudinal position of the South China Craton (reference site at 31.0 °N, 110.0 °E) during the Middle Triassic, Early-Middle Jurassic (Zhao et al., 2020) and Late Jurassic (Lin et al., 1985; Bai et al., 1998; Wu et al., 1999; Yokoyama et al., 1999, 2001, Yi et al., 2019) based on paleomagnetic research. The fourth Late Jurassic data point was refined by inclination flattening correction (IF correction factor of f = 0.6) according to Zhao et al. (2020). Detailed paleomagnetic data are listed in Table S7. Red and gray arrows in A and B represent long-term variations in PCO_2 and CIA_{corr} during the Triassic and Jurassic, respectively. Green and red in (C) represent the high-latitude/equator humid zone and low- to mid-latitude arid zone (Kent et al., 2017; Muttoni et al., 2013), respectively. (For interpretation of the references to colour in this figure legend, the reader is referred to the web version of this article.)

Nesbitt and Young, 1982), which is incompatible with the average PCO_2 in the ice-free Triassic and Jurassic that measures four times the preindustrial PCO_2 levels. Regarding the joint influence of water availability and mean annual temperature on chemical weathering (Rasmussen et al., 2011), the decoupling of PCO_2 (mean annual temperature indicator) from CIA_{corr} implies that other driving mechanisms such as humidity also contributed to the observed climate and chemical weathering changes in the region.

6.5.2. *Megamonsoon effect*

The Pangaea supercontinent formed during the late Permian and dominated the tectonics and paleogeography in the Triassic–Jurassic. This supercontinent extended from the equator to polar regions and surrounded the Tethys Ocean at middle to low latitudes. This unique supercontinent configuration and the Mesozoic greenhouse period resulted in the greatest thermal contrasts between the winter and summer hemispheres, which generated seasonal reversal of surface wind and hydrologic cycle directions and the most intensive single monsoonal climate system in geological history, leading to the seasonal climate in the circum-Tethyan region of Pangaea and severe year-round drought in the vast supercontinent interior (Kutzbach and Gallimore, 1989; Parrish, 1993; Fang et al., 2016). This intense monsoonal system was first named the 'megamonsoon' by Pamela Robinson in 1973 based on conceptual models and has also has been demonstrated by azonal climate belt reconstructions (Parrish et al., 1982; Hallam, 1985), climate simulations (Wilson et al., 1994; Sellwood and Valdes, 2006) and sedimentological evidence (Clemmensen et al., 1998; Scherer and Goldberg, 2007; Zeng et al., 2019). As Pangaea moved north, the supercontinent was symmetrically divided by the equator, which caused maximum pressure contrasts between the Northern and Southern Hemispheres during the Late Triassic (Parrish, 1993), at which time the megamonsoon intensity reached its peak. Climate simulations (Chandler et al., 1992) and conceptual models (Parrish, 1993; Fang et al., 2016) have shown that a monsoon system still existed during the Early Jurassic in Southeast Asia, which was characterized by a perennially wet climate due to continuous moisture transport by cyclones in the summer over the Tethys Ocean and anticyclones in winter over the Panthalassa. The megamonsoon weakened and finally collapsed with the break-up of Pangaea after the Late Jurassic.

Direct evidence for the monsoonal effect in the study region comes from monsoonal paleosol depositions in the Xiakou Section. We found several calcisol segments in the Middle to Upper Jurassic strata with very thick and diffused Bk horizons with a maximum thickness of ~1.5–2 m (Fig. 3I), even without correcting for compaction. Although the megamonsoon was regarded as already weakened after the Late Triassic (Parrish, 1993), these thicknesses still matched and even exceeded the critical Bk thickness of ~1 m for most modern monsoonal tropical soils in India, Iraq and Tanzania (Retallack, 2005), which implies an obvious monsoonal influence over the South China Craton, which was located at the low-middle latitudes of the eastern Tethys during the Early Mesozoic. The megamonsoon would also have led to fierce atmospheric circulation activity (e.g., storms) that occurring at

higher latitudes than modern atmospheric circulation activity. This is supported by abundant Middle Triassic marine tempestites in the western margin of the South China Craton (Feng et al., 2017) and Zigui Basin (Fig. 3A–B) in South China and coeval semiprecession signals in lacustrine sediments from the Ordos Basin at higher latitudes in inland North China (Chu et al., 2020). However, the climatic indices and CMZs from the lower to middle part of the Badong Formation record mainly arid climate conditions during the Middle–early Late Triassic, probably because the megamonsoon system had not yet formed completely. The variable chemical weathering records during this period may be related to perturbations in monsoon intensity and, hence, the precipitation pattern.

From the Late Triassic–Early Jurassic, the Cimmerian and Indosinian orogenies resulted in widespread tectonic uplift, which would have also enhanced the megamonsoon in the eastern Tethys because the thermal properties of high mountains led airflow to migrate farther inland (Parrish, 1993). Late Triassic tempestites and trace fossils (Pole et al., 2018; Lu et al., 2019) and the results of tree-ring studies in the Sichuan Basin (Qian et al., 2010; Deng et al., 2017b) consistently indicate an enhanced monsoon-driven, high-energy environment and seasonal climate in mid-latitude South China (approximately 34–40°N). As such, the gradually increasing weathering intensity in the uppermost Badong Formation (Fig. 7) was a positive response to strengthening monsoonal processes in the eastern Tethys region, as these processes delivered copious monsoonal rains from both the Tethys and Panthalassic Oceans and led to a dominant perennially wet climate and intense chemical weathering during the Latest Triassic–early Middle Jurassic (Fig. 7).

The collapse of the megamonsoon system after the Late Jurassic hindered onshore moisture transport and caused a drier climate in the original circum-Tethys monsoon region, including in South China. However, this mechanism cannot solely account for the drier climate and weakened chemical weathering in the study area, as these processes occurred earlier than expected during the early Middle Jurassic. Meanwhile, monsoonal calcisol depositions and CMZ III imply that a strong seasonal climate still affected the study area during the early Late Jurassic, even after aridification (Fig. 3I; Fig. 7). Thus, the megamonsoon cannot entirely explain the climate change and another climate-driving mechanism is still required.

6.5.3. *Movement of the Asian region across zonal climate belts*

Prior to and after the Late Triassic megamonsoon peak stage, planetary winds were dominated by the heterogeneity of latitudinal insolation, which affected the global climate and formed zonal climate belts. At this time, a narrow tropical humid climate zone was limited to 5° on either side of the paleoequator, broad arid belts extended to 30°N/S, and humid zones were distributed in the middle to high latitudes above 80°N/S (Muttoni et al., 2013; Kent et al., 2017, Fig. 8C).

After correcting the inclination flattening (IF) influence on the previous paleomagnetic data of clastic rocks, Zhao et al. (2020) recalculated the paleomagnetic poles of the South China Craton based on the site average of nine available high-quality (Quality factor $\geq$ 4) paleomagnetic pole datapoints to determine the paleoposition of the South China Craton from the Middle Triassic to Middle Jurassic, suggesting that the South China Craton was located at a low paleolatitude of 14.1 $\pm$ 9.1°N at the reference site (33.0°N, 109.5°E), which was slightly north of the studied Zigui and Dangyang Basins (reference site: 31.0°N, 110° E) during the Middle Triassic, resulting in an arid baseline climate and weak chemical weathering in the study area during this period (Fig. 8C and Fig. 9A). Despite a lack of qualified Late Triassic paleomagnetic data, the paleoposition reconstruction results of 39.4 $\pm$ 4.5°N for the South China Craton in the early Early–Middle Jurassic (Fig. 8C) implied the continuous northward drift of South China after the Middle Triassic, which moved the study area into a mid-latitude humid belt affected by the megamonsoon system during its peak in the latest Triassic and Early Jurassic (Fig. 9B). This caused intense chemical weathering due to the humid climate, as recorded by the weathering and climatic indices and clay mineral assemblages in the Jiuligang, Tongzhuyuan and lowermost Qianfoya formations (Fig. 7).

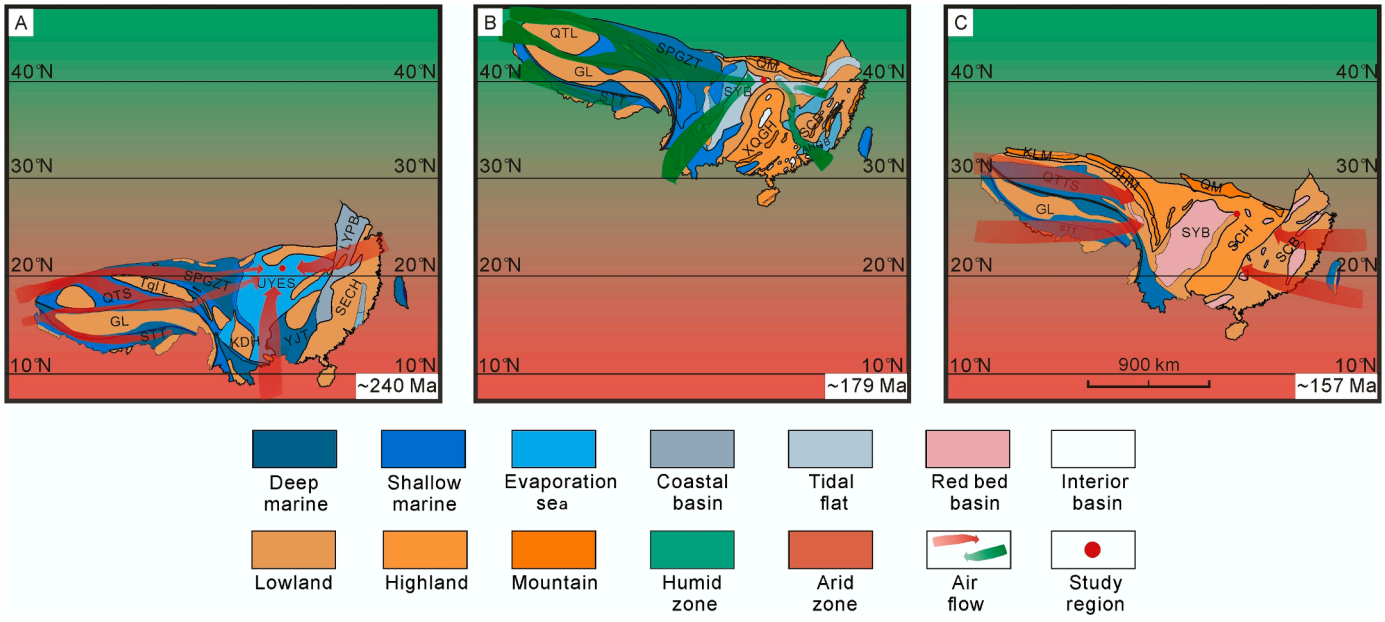

Fig. 9. Paleogeographic map and main atmospheric circulation directions in the South China region in eastern Pangaea during the (A) Middle Triassic (~240 Ma), (B) Early Jurassic (~179 Ma) and (C) Late Jurassic (~157 Ma), as modified from Wang et al. (1985) and based on plate paleoposition in Fig. 8C. The positions of the low- to mid-latitude arid zone and high-latitude humid zone were taken from Kent et al. (2017) and Muttoni et al. (2013). The drift of the South China Craton was taken from Golonka (2007), Huang et al. (2018), and Yi et al. (2019). Abbreviations: QTS = Qiangtang Shallow Marine, QTL = Qiangtang Lowland, GL = Gangdese Lowland, SECH = Southeast China Hill Region, STT = South Tibet Trough, TglL = Tangugula Lowland, SPGZT = Songpan–Ganzi Trough, KDH = Kangdian (Sichuan–Yunnan) Hill Region, UYES = Upper Yangtze Evaporitic Sea, YJT = Youjiang Trough, LYPB = Lower Yangtze Paralic Basin, SYB = Sichuan–Yunnan Basin, XQGH = Xiang–Qian–Gui (Hunan–Guizhou–Guangxi) Highland, SCB = South China Basin, SCH = South China Highland, QM = Qinling Mountains, KM = Kunlun Mountains, and BHM = Bayan Har Mountains.

During the Middle-Late Jurassic, paleomagnetic data indicate that the Eastern Asia blocks (EABs) moved southward by ~25° sometime between 174 ± 6 Ma and 157 ± 4 Ma through true polar wandering, thus leading to a much drier climate. This is known as the Great Jurassic East Asian Aridification event and occurred over an area of 10×10^6 km^2 (Yi et al., 2019). Based on the paleolatitude of 36.6 ± 5.1°N for the North China Craton (reference site 40°N, 120°E) at 157 ± 4 Ma, the recalculated paleoposition of the study region in South China was ~27°N. This finding is compatible with the result of 30.5 ± 8.3°N, which was averaged from five Late Jurassic high-quality paleomagnetic pole data points (Fig. 8C, Lin et al., 1985; Bai et al., 1998; Wu et al., 1999; Yokoyama et al., 1999, 2001) following the method of Zhao et al. (2020).This shift resulted in weak chemical weathering and other changes in the clay mineral assemblages in the lowermost Qianfoya Formation in the Xiakou section (Fig. 7) because the large-scale southward drift of the EABs moved South China from the mid- to high-latitude humid belt back to the low-latitude arid belt, where it was located during the Middle Triassic (Fig. 9C). As such, the megamonsoon system regained control of the regional climate conditions, which is consistent with the abundant mixed I/S in the Qianfoya Formation. Some previous studies have reported several abrupt decreases in seawater temperature during the Middle–Late Jurassic in the western Tethys region (Dromart et al., 2003; Korte et al., 2015; Bodin et al., 2020), with the potential to trigger weakened continental weathering, but whether these cold events had an impact beyond the western Tethys region is still controversial (Wierzbowski et al., 2018; Alberti et al., 2020). Even if these cold events did occur, the equatorward movement of South China during the Middle Jurassic would have largely counteracted their influence on the weathering record of the samples analyzed in this study.

6.5.4. Regional paleogeographic evolution

Regional paleogeography could also have had a significant impact on the paleoclimate in the study area. During the Triassic, a Paleo-Tethys-type epeiric sea covered a large area of South China from the west. Moreover, Lower Jurassic estuarine deposits in the Fujian–Guangdong–Jiangxi–Hunan Provinces (Xu et al., 2012) imply a vast Panthalassa-type coastal environment along the southern margin of South China, and there were also no large mountain ranges between the Middle–Lower Yangtze area and Panthalassa in the east (Wang et al., 1985). Therefore, the study area was surrounded by seas on three sides and received copious oceanic moisture, and these conditions led to a humid climate in the Late Triassic to the Early Jurassic (Fig. 9B). However, Indosinian tectonism began in the Late Triassic and caused the gradual closure of the Paleo-Tethys Ocean, uplifting most of South China and forming the Songpan–Ganze Fold Belt and Bayan Har Mountains in western South China (Roger et al., 2010; Shao et al., 2014). Ultimately, these processes prevented moisture transport to the northern margin of South China from the Tethys Ocean after the Middle Jurassic. Similarly, moisture transport from the Panthalassa in the south to the study area weakened because of the subduction and compression of the circum-Pacific tectonic domain after the Middle Jurassic. This process led to regression of the Panthalassa coastal environment along the southeastern margin of South China. The transition from Indosinian to Yanshanian tectonism during the early Middle Jurassic caused widespread overthrusting and folding in North and South China, and at this time, South China was divided into the Sichuan Basin and a neighboring continental red basin area in the west and a basin-and-range area in the east, isolating the study area from the effects of Panthalassic ocean currents (Wang et al., 1985; Liu et al., 2014; Luo et al., 2014). Subsequently, the study area was unaffected by the surrounding oceans, and this isolation enhanced inland drought conditions after the Middle–Late Jurassic (Fig. 9C).

7. Conclusions

Multiple chemical weathering and climatic indices and clay mineralogy were used in this study to reconstruct the paleoclimate from the Middle Triassic to the Late Jurassic on the northern margin of the South China Craton.

During the Middle–early Late Triassic, an arid climate existed, as evidenced by low chemical weathering index values and clay mineral assemblages of mainly illite and chlorite. Relatively high CIA_{corr} values measured in the Jiuligang and Tongzhuyuan formations and the occurrence of kaolinite in the Tongzhuyuan Formation indicated increased humidity from the latest Triassic to the Early Jurassic. This humid environment persisted until the early Middle Jurassic, when abrupt weakening of chemical weathering occurred, implying that the climate became seasonally dry and humid beginning in the Middle Jurassic. Uniformly low chemical weathering index values and increased illite amounts indicate enhanced drought conditions after the Middle Jurassic through the Late Jurassic.

The long-term climate evolution of the climate and changes in chemical weathering in the study area were controlled by multiple factors, including PCO_2 variations, the megamonsoon system and the drift of the South China Plate across zonal climate belts during the Middle Triassic to the Late Jurassic. In addition, the topographic evolution in response to tectonism also had an important influence on the climate by affecting ocean–land water transport, further enhancing the interior drought conditions after the Middle Jurassic.

Declaration of Competing Interest

The authors declare that they have no known competing financial interests or personal relationships that could have appeared to influence the work reported in this paper.

Acknowledgments

We are grateful for the help from Delin Song, Chunlei Zhao and Yuhui Sun in the field and Dr. Ke Yin, Kaipeng Ji and Chenlei Zhao in the laboratory. We thank Prof. Yajun Xu, Dr. Jianghai Yang and Dr. Wenchao Yu for their helpful discussion, Dr. Tinghong Zhou for her help with paleomagnetic data processing and Dr. Bas Van de Schootbrugge for his comment on a draft of the manuscript. We also thank Prof. Thomas Algeo and two anonymous reviewers for their constructive comments, which greatly improved this paper. This study was financially supported by the Natural Science Foundation of China (Grant Nos. 41672106) and the International Exchange and Cooperation Funding Program of Graduate School, China University of Geosciences (Wuhan).

Appendix A. Supplementary data

Supplementary data to this article can be found online at https://doi.org/10.1016/j.palaeo.2021.110744.

References

Alberti, M., Fürsich, F.T., Andersen, N., 2019. First steps in reconstructing Early Jurassic sea water temperatures in the Andean Basin of northern Chile based on stable isotope analyses of oyster and brachiopod shells. J. Palaeogeogr. 8. https://doi.org/10.1186/s42501-019-0048-0.

Alberti, M., Leshno, Y., Fürsich, F.T., Edelman-Furstenberg, Y., Andersen, N., Garbe-Schönberg, D., 2020. Stress in the tropics? Impact of a latitudinal seawater δ18O gradient on Middle Jurassic temperature reconstructions at low latitudes. Geology. https://doi.org/10.1130/g47824.1.

Bai, L.X., Zhu, R.X., Wu, H.N., Guo, B., 1998. Paleomagnetism of the Late Jurassic northern Sichuan Basin and preliminary study on the true wander. Acta Geol. Sin. 41 (3), 324–331 (in Chinese with English abstract).

Beerling, D.J., Berner, R.A., 2002. Biogeochemical constraints on the Triassic-Jurassic boundary carbon cycle event. Glob. Biogeochem. Cycles 16. https://doi.org/10.1029/2001GB001637, 10-11-10-13.

Berner, R.A., Kothavala, Z., 2001. GEOCARB III: A revised model of atmospheric CO2 over phanerozoic time. Am. J. Sci. 301, 182–204. https://doi.org/10.2475/ajs.301.2.182.

Biscaye, P.E., 1965. Mineralogy and sedimentation of recent deep-Sea Clay in the Atlantic Ocean and Adjacent Seas and Oceans. Geol. Soc. Am. Bull. 76 https://doi.org/10.1130/0016-7606(1965)76[803:Masord]2.0.Co;2.

Bodin, S., Mau, M., Sadki, D., Danisch, J., Nutz, A., Krencker, F.-N., Kabiri, L., 2020. Transient and secular changes in global carbon cycling during the early Bajocian event: Evidence for Jurassic cool climate episodes. Glob. Planet. Chang. https://doi.org/10.1016/j.gloplacha.2020.103287.

Bouchez, J., Gaillardet, J., France-Lanord, C., Maurice, L., Dutra-Maia, P., 2011. Grain size control of river suspended sediment geochemistry: clues from Amazon River depth profiles. Geochem. Geophys. Geosyst. 12 https://doi.org/10.1029/2010gc003380.

Boucot, A.J., Chen, X., Scotese, C.R., 2013. Phanerozoic Paleoclimate: An Atlas of Lithologic Indicators of Climate.

Cao, J., Wu, M., Chen, Y., Hu, K., Bian, L., Wang, L., Zhang, Y., 2012. Trace and rare earth element geochemistry of Jurassic mudstones in the northern Qaidam Basin, northwest China. Chem. Erde Geochem. 72, 245–252. https://doi.org/10.1016/j.chemer.2011.12.002.

Casacci, M., Bertinelli, A., Algeo, T.J., Rigo, M., 2016. Carbonate-to-biosilica transition at the Norian-Rhaetian boundary controlled by rift-related subsidence in the western Tethyan Lagonegro Basin (southern Italy). Palaeogeogr. Palaeoclimatol. Palaeoecol. 456, 21–36. https://doi.org/10.1016/j.palaeo.2016.05.007.

Chai, R., Yang, J., Du, Y., Ding, D., 2016. Middle Triassic- Early Jurassic Sedimentary Record in th Zigui Basin and Implication for the Qinling Indosinian Collisional Orogensis. Geol. Sci. Technol. Informat. 43–49 (in Chinese with English Abstract).

Chamley, H., 1980. Clay Sedimentation and Paleoenvironment in the Area of Daito Ridge (Northwestern Philippine Sea) since the Early Eocene. Initial Reports of the Deep Sea Drilling Project, vol. 85. U.S. Government Printing Office, Washington, pp. 683–690.

Chandler, M.A., Rind, D., Ruedy, R., 1992. Pangaean Climate during the Early Jurassic - GCM Simulations and the Sedimentary Rrcord of Paleoclimate. Geol. Soc. Am. Bull. 104, 543–559. https://doi.org/10.1130/0016-7606(1992)104<0543:PCDTEJ>2.3.CO;2.

Chen, H.S., Zhang, Z.L., 2002. Sporopollen Assemblage of the Middle Jurassic Xietan Formation in the Zigui Basin, Hubei. Acta Micropalaepntol. Sinca 19, 301–308 (in Chinese with English Abstract).

Chen, H.M., Zhang, Z.L., 2004. Discovery of the Middle Jurassic Sporopollen Assembage in the Chenjiwan Formation of Zigui Basin, Hubei and its Significance. Acta Micropalaepntol. Sinca 21, 199–208 (in Chinese with English Abstract).

Chen, H.M., Meng, F.S., Zhang, Z.L., 2002. Lectostratotype section of The Early Jurassic Xiangxi Formation in Zigui Basin of Western Hubei. J. Stratigr. 26, 187-192+234 (in Chinese with English Abstract).

Chu, R., Wu, H., Zhu, R., Fang, Q., Deng, S., Cui, J., Yang, T., Li, H., Cao, L., Zhang, S., 2020. Orbital forcing of Triassic megamonsoon activity documented in lacustrine sediments from Ordos Basin, China. Palaeogeogr. Palaeoclimatol. Palaeoecol. 541 https://doi.org/10.1016/j.palaeo.2019.109542.

Clemmensen, L.B., Kent, D.V., Jenkins, F.A., 1998. A Late Triassic lake system in East Greenland: facies, depositional cycles and palaeoclimate. Palaeogeogr. Palaeoclimatol. Palaeoecol. 140, 135–159. https://doi.org/10.1016/S0031-0182(98)00043-1.

Deng, S., Lu, Y., Zhao, Y., Fan, R., Wang, Y., Yang, X., Li, X., Sun, B., 2017a. The Jurassic palaeoclimate regionalization and evolution of China. Earth Sci. Front. 24, 106–142.

Deng, S., Zhao, Y., Lu, Y.Z., Shang, P., Fan, R., Li, X., Dong, S.X., Liu, L., 2017b. Plant fossils from the Lower Jurassic coal-bearing formation of central Inner Mongolia of China and their implications for palaeoclimate. Palaeoworld 26, 279–316. https://doi.org/10.1016/j.palwor.2017.01.003.

Dera, G., Brigaud, B., Monna, F., Laffont, R., Puceat, E., Deconinck, J.-F., Pellenard, P., Joachimski, M.M., Durlet, C., 2011. Climatic ups and downs in a disturbed Jurassic world. Geology 39, 215–218. https://doi.org/10.1130/g31579.1.

Dong, Y., Santosh, M., 2016. Tectonic architecture and multiple orogeny of the Qinling Orogenic Belt, Central China. Gondwana Res. 29, 1–40. https://doi.org/10.1016/j.gr.2015.06.009.

Dromart, G., Garcia, J.P., Picard, S., Atrops, F., Lecuyer, C., Sheppard, S.M.F., 2003. Ice age at the Middle-Late Jurassic transition? Earth Planet. Sci. Lett. 213, 205–220. https://doi.org/10.1016/s0012-821x(03)00287-5.

Fang, X., Song, C., Yan, M., Zan, J., Liu, C., Sha, J., Zhang, W., Zeng, Y., Wu, S., Zhang, D., 2016. Mesozoic litho- and magneto-stratigraphic evidence from the central Tibetan Plateau for megamonsoon evolution and potential evaporites. Gondwana Res. 37, 110–129. https://doi.org/10.1016/j.gr.2016.05.012.

Fedo, C.M., Nesbitt, H.W., Young, G.M., 1995. Unraveling the effectsof Potassium Metasomatism in Sedimentary-Rocks and Paleosols, with Implications for Paleoweathering Conditions and Provenance. Geology 23, 921–924. https://doi.org/10.1130/0091-7613(1995)023<0921:Uteopm>2.3.Co;2.

Feng, X., Chen, Z.-Q., Woods, A., Pei, Y., Wu, S., Fang, Y., Luo, M., Xu, Y., 2017. Anisian (Middle Triassic) marine ichnocoenoses from the eastern and western margins of the Kamdian Continent, Yunnan Province, SW China: implications for the Triassic biotic recovery. Glob. Planet. Chang. 157, 194–213. https://doi.org/10.1016/j.gloplacha.2017.09.004.

Foster, G.L., Royer, D.L., Lunt, D.J., 2017. Future climate forcing potentially without precedent in the last 420 million years. Nat. Commun. 8, 14845. https://doi.org/10.1038/ncomms14845.

Fu, X., Wang, J., Zeng, S., Feng, X., Wang, D., Song, C., 2017. Continental weathering and palaeoclimatic changes through the onset of the Early Toarcian oceanic anoxic event in the Qiangtang Basin, eastern Tethys. Palaeogeogr. Palaeoclimatol. Palaeoecol. 487, 241–250. https://doi.org/10.1016/j.palaeo.2017.09.005.

Gao, S., Luo, T.C., Zhang, B.R., Zhang, H.F., Han, Y.W., Zhao, Z.D., Hu, Y.K., 1998. Chemical composition of the continental crust as revealed by studies in East China. Geochim. Cosmochim. Acta 62, 1959–1975. https://doi.org/10.1016/S0016-7037(98)00121-5.

Garzanti, E., Padoan, M., Peruta, L., Setti, M., Najman, Y., Villa, I.M., 2013. Weathering geochemistry and Sr-Nd fingerprints of equatorial upper Nile and Congo muds. Geochem. Geophys. Geosyst. 14, 292–316. https://doi.org/10.1002/ggge.20060.

Gernon, T.M., Hincks, T.K., Merdith, A.S., Rohling, E.J., Palmer, M.R., Foster, G.L., Bataille, C.P., Müller, R.D., 2021. Global chemical weathering dominated by continental arcs since the mid-Palaeozoic. Nat. Geosci. 14, 690–696. https://doi.org/10.1038/s41561-021-00806-0.

Golonka, J, 2007. Late Triassic and Early Jurassic palaeogeography of the world. Palaeogeogr. Palaeoclimatol. Palaeoecol. 244, 297–307. https://doi.org/10.1016/j.palaeo.2006.06.041.

Golonka, J., Embry, A., Krobicki, M., 2018. Late Triassic Global Plate Tectonics. In: The Late Triassic World, pp. 27–57.

Gomez, J.J., Comas-Rengifo, M.J., Goy, A., 2016. Palaeoclimatic oscillations in the Pliensbachian (Early Jurassic) of the Asturian Basin (Northern Spain). Clim. Past 12, 1199–1214. https://doi.org/10.5194/cp-12-1199-2016.

Grossman, E.L., 2012. Geological Time Scale 2012. Chapter 10. Oxygen isotope stratigraphy, Appendix 1, Supplement to: Grossman, EL (2012): Oxygen isotope stratigraphy (chapter 10). In: Gradstein, F., Ogg, J. (Eds.), Geological time Scale 2012 2-Volume Set, 1st Edition, Elsevier, ISBN: 9780444594259 (PANGAEA).

Hagen, C.J., Roberts, E.M., Sullivan, C., Liu, J., Wang, Y., Agyemang, P.C.O., Xu, X., 2018. Taphonomy, Geological Age, and Paleobiogeography of Lotosaurus Adentus (Archosauria: Poposauroidea) From the Middle -Upper Triassic Badong Formation, Hunan, China. Palaios 33, 106–124. https://doi.org/10.2110/palo.2017.084.

Hallam, A., 1985. A Review of Mesozoic Climates. J. Geol. Soc. 142, 433–445. https://doi.org/10.1144/gsjgs.142.3.0433.

Harnois, L., 1988. The CIW index - a new chemical index of weathering. Sediment. Geol. 55, 319–322. https://doi.org/10.1016/0037-0738(88)90137-6.

Harris, R., McCall, R., Randall, O., Bin Tawang, M.H., Williams, R., Fairman, J.G., Schultz, D.M., 2017. Climate change during the Triassic and Jurassic. Geol. Today 33, 210–215. https://doi.org/10.1111/gto.12210.

Holz, M., 2015. Mesozoic paleogeography and paleoclimates – A discussion of the diverse greenhouse and hothouse conditions of an alien world. J. S. Am. Earth Sci. 61, 91–107. https://doi.org/10.1016/j.jsames.2015.01.001.

Hu, J., Ma, Y., Wang, Z., Liu, Y., Gao, W., Qian, T., 2017. Palaeoenvironment and palaeoclimate of the Middle to Late Jurassic revealed by geochemical records in northern margin of Qaidam Basin. J. Palaeogeogr. 19, 480–490. https://doi.org/10.7605/gdlxb.2017.03.037.

Huang, B., Yan, Y., Piper, J.D.A., Zhang, D., Yi, Z., Yu, S., Zhou, T., 2018. Paleomagnetic constraints on the paleogeography of the East Asian blocks during Late Paleozoic and Early Mesozoic times. Earth Sci. Rev. 186, 8–36. https://doi.org/10.1016/j.earscirev.2018.02.004.

Jenkyns, H.C., 1988. The Early Toarcian (Jurassic) Anoxic Event - Stratigraphic, Sedimentary, and Geochemical Evidence. Am. J. Sci. 288, 101–151. https://doi.org/10.2475/ajs.288.2.101.

Jenkyns, H., Schouten-Huibers, L., Schouten, S., Sinninghe Damsté, J.J.C.o.t.P, 2012. Warm Middle Jurassic–Early Cretaceous high-latitude sea-surface temperatures from the Southern Ocean. Clim. Past 8, 215–226. https://doi.org/10.5194/cp-8-215-2012.

Jian, X., Guan, P., Zhang, W., Feng, F., 2013. Geochemistry of Mesozoic and Cenozoic sediments in the northern Qaidam basin, northeastern Tibetan Plateau: implications for provenance and weathering. Chem. Geol 74–88. https://doi.org/10.1016/j.chemgeo.2013.10.011 s 360–361.

Jiang, H.S., Yuan, J.L., Chen, Y., Ogg, J.G., Yan, J.X., 2019. Synchronous onset of the Mid-Carnian Pluvial Episode in the East and West Tethys: Conodont evidence from Hanwang, Sichuan, South China. Palaeogeogr. Palaeoclimatol. Palaeoecol. 520, 173–180. https://doi.org/10.1016/j.palaeo.2019.02.004.

Kamei, A., Fukushi, K., Takagi, T., Tsukamoto, H., 2012. Chemical overprinting of magmatism by weathering: A practical method for evaluating the degree of chemical weathering of granitoids. Appl. Geochem. 27, 796–805. https://doi.org/10.1016/j.apgeochem.2011.12.014.

Kenny, R., 2017. A cool time in the Early Jurassic: first continental palaeoclimate estimates from oxygen and hydrogen isotope ratios in chert from Navajo Sandstone carbonate lenses, Utah (USA). Carbonates Evaporites 32, 45–52. https://doi.org/10.1007/s13146-015-0276-z.

Kent, D.V., Olsen, P.E., Muttoni, G., 2017. Astrochronostratigraphic polarity time scale (APTS) for the Late Triassic and Early Jurassic from continental sediments and correlation with standard marine stages. Earth Sci. Rev. 166, 153–180. https://doi.org/10.1016/j.earscirev.2016.12.014.

Kidder, D.L., Worsley, T.R., 2010. Phanerozoic large igneous provinces (LIPs), HEATT (haline euxinic acidic thermal transgression) episodes, and mass extinctions. Palaeogeogr. Palaeoclimatol. Palaeoecol. 295 (1), 162–191. https://doi.org/10.1016/j.palaeo.2010.05.036.

Korte, C., Hesselbo, S.P., Ullmann, C.V., Dietl, G., Ruhl, M., Schweigert, G., Thibault, N., 2015. Jurassic climate mode governed by ocean gateway. Nat. Commun. 6. https://doi.org/10.1038/ncomms10015.

Kutzbach, J.E., Gallimore, R.G., 1989. Pangaean climate-megamonsoons of the megacontinent. J. Geophys. Res.-Atmos. 94, 3341–3357. https://doi.org/10.1029/JD094iD03p03341.

Lécuyer, C., Picard, S., Garcia, J.-P., Sheppard, S.M.F., Grandjean, P., Dromart, G., 2003. Thermal evolution of Tethyan surface waters during the Middle-Late Jurassic: evidence from δ18O values of marine fish teeth. Paleoceanography 18. https://doi.org/10.1029/2002pa000863 n/a-n/a.

Lerman, A., 1978. Lakes: Chemistry, geology, physics., x + 363 p. Springer-Verlag. New York, Heidelberg, Berlin.

Li, M., Huang, C., Hinnov, L., Chen, W., Ogg, J., Tian, W., 2018. Astrochronology of the Anisian stage (Middle Triassic) at the Guandao reference section, South China. Earth Planet. Sci. Lett. 482, 591–606. https://doi.org/10.1016/j.epsl.2017.11.042.

Li, L., Wang, Y., Kürschner, W.M., Ruhl, M., Vajda, V., 2020. Palaeovegetation and palaeoclimate changes across the Triassic–Jurassic transition in the Sichuan Basin, China. Palaeogeogr. Palaeoclimatol. Palaeoecol. 556 https://doi.org/10.1016/j.palaeo.2020.109891.

Lin, L.J., Fuller, M., Zhang, W.Y., 1985. Preliminary Phanerozoic polar wander paths for the North and South China blocks. Nature 313, 444–449. https://doi.org/10.1038/313444a0.

Liu, S., Steel, R., Zhang, G., 2005. Mesozoic sedimentary basin development and tectonic implication, northern Yangtze Block, eastern China: record of continent–continent collision. J. Asian Earth Sci. 25, 9–27. https://doi.org/10.1016/j.jseaes.2004.01.010.

Lin, W.B., Shang, Y.K., 1980. Sporo-Pollen assemblages from the Mesozoic Coal Series of Western Hubei. Acta Palaeontol. Sin. 19, 201–219 (in Chinese with English Abstract). https://doi.org/10.19800/j.cnki.aps.1980.03.004.

Liu, Y.Q., Kuang, H.W., Peng, N., Xu, H., Zhang, P., An, W., Wang, N.S., Zhu, Z.C., Fan, Z. X., 2014. Depositional and paleogeographic evolution of Mesozoic continental facies in China. In: The 13th National Conference of Palaeogeography and Sediemntology, Beijing, China, pp. 33–34.

Lu, N., Wang, Y., Popa, M.E., Xie, X., Li, L., Xi, S., Xin, C., Deng, C., 2019. Sedimentological and paleoecological aspects of the Norian–Rhaetian transition (Late Triassic) in the Xuanhan area of the Sichuan Basin, Southwest China. Palaeoworld. https://doi.org/10.1016/j.palwor.2019.04.006.

Luo, M.S., Lu, L.Q., Jia, J., Wang, S.D., Xu, Y.D., He, W.H., 2014. Evolution of Sedimentary Basins in China during Mesozoic. Earth Sci. J. China Univ. Geosci. 39, 954–976 (in Chinese with English Abstract). https://doi.org/10.3799/dqkx.2014.088.

Ma, Q.L., Chai, R., Du, Y.S., Yang, J.H., Dai, X.D., 2019. Geochronological Constraints on Tuffs of the Badong Formation along the North Margin of the Middle Yangtze region, 93, pp. 2785–2796 (in Chinese with English Abstract). 10.19762/j.cnki.dizhixuebao.2019195.

Manabe, S., Wetherald, R.T., 1980. On the distribution of climate change resulting from an increase in CO2 content of the atmosphere. J. Atmos. Sci. 37, 99–118 doi: 10.1175/1520–0469(1980)037<0099:OTDOCC>2.0.CO;2.

McElwain, J.C., Beerling, D.J., Woodward, F.I., 1999. Fossil plants and global warming at the Triassic-Jurassic boundary. Science 285, 1386–1390. https://doi.org/10.1126/science.285.5432.1386.

McLennan, S.M., 1993. Weathering and Global Denudation. J. Geol. 101, 295–303. https://doi.org/10.1086/648222.

Meng, F.S., 1999. Middle Jurassic fossil plant in the Yangtze Gorges Area of China and their Paleo-Climatic environment. Geol. Miner. Resour. South China 19–26 (in Chinese with English Abstract).

Meng, F.S., 2007. Stratigraphic Division of the bottom Jurassic in Zigui Basin, West Hubei, The 24th Annual Meeting of Palaeontological Society of China. Pingyi, Shandong, China, pp. 55–56 (in Chinese without English Abstract).

Meng, F.S., 2010. Stratigraphic Division and Correlation of the Marine and Continental Jurassic System in South China. Geol. Miner. Resour. South China 55–65 (in Chinese with English Abstract).

Meng, F.S., Li, X.B., 2003. Meticulous correlation of upper triassic series on the Eastern and Western Limbs of the Huangling Dome, Western Hubei. Geol. Miner. Resour. South China 60–65 (in Chinese with English Abstract).

Meng, F.S., Zhang, Z.L., Sheng, X.C., 1995. The triassic-jurassic stratigraphy, palaeoeclogy and palaeoclimatology in the Yangtze Gorge Area. Proceed. Stratigr. Palaeontol. 25, 107–131 (in Chinese with English Abstract).

Meunier, A., Caner, L., Hubert, F., El Albani, A., Pret, D., 2013. The weathering intensity scale (WIS): An alternative approach of the Chemical Index of Alteration (CIA). Am. J. Sci. 313, 113–143. https://doi.org/10.2475/02.2013.03.

Moore, D.M., Reynolds, R.C., 1989. X-ray Diffraction and the Identification and Analysis of Clay Minerals. Oxford University Press, Oxford, p. 332.

Muttoni, G., Dallanave, E., Channell, J.E.T., 2013. The drift history of Adria and Africa from 280 Ma to Present, Jurassic true polar wander, and zonal climate control on Tethyan sedimentary facies. Palaeogeogr. Palaeoclimatol. Palaeoecol. 386, 415–435. https://doi.org/10.1016/j.palaeo.2013.06.011.

Nesbitt, H.W., Young, G.M., 1982. Early proterozoic climates and plate motions inferred from Major Element Chemistry of Lutites. Nature 299, 715–717. https://doi.org/10.1038/299715a0.

Nesbitt, H.W., Young, G.M., 1984. Prediction of some Weathering Trend of Plutonic and Volcanic-Rocks Based on Thermodynamic and Kinetic Considerations. Geochim. Cosmochim. Acta 48, 1523–1534. https://doi.org/10.1016/0016-7037(84)90408-3.

Nordt, L., Atchley, S., Dworkin, S., 2015. Collapse of the Late Triassic megamonsoon in western equatorial Pangea, present-day American Southwest. Geol. Soc. Am. Bull. 127, 1798–1815. https://doi.org/10.1130/b31186.1.

Pálfy, J., Smith, P.L., 2000. Synchrony between Early Jurassic extinction, oceanic anoxic event, and the Karoo-Ferrar flood basalt volcanism. Geology 28. https://doi.org/10.1130/0091-7613(2000)28<747:Sbejeo>2.0.Co;2.

Panahi, A., Young, G.M., Rainbird, R.H., 2000. Behavior of major and trace elements (including REE) during Paleoproterozoic pedogenesis and diagenetic alteration of an Archean granite near Ville Marie, Quebec, Canada. Geochim. Cosmochim. Acta 64, 2199–2220. https://doi.org/10.1016/s0016-7037(99)00420-2.

Parker, A., 1970. An index of weathering for silicate rocks. Geol. Mag. 107, 501–504 doi: 10.1017/S0016756800058581.

Parrish, J.T., 1993. Climate of the Supercontinent Pangaea. J. Geol. 101, 215–233. https://doi.org/10.1086/648217.

Parrish, J.T., Ziegler, A.M., Scotese, C.R., 1982. Rainfall patterns and the distribution of coals and evaporaporites in the Mesozoic and Cenozoic. Palaeogeogr. Palaeoclimatol. Palaeoecol. 40, 67–101. https://doi.org/10.1016/0031-0182(82)90085-2.

Perri, F., 2018. Reconstructing chemical weathering during the Lower Mesozoic in the Western-Central Mediterranean area: a review of geochemical proxies. Geol. Mag. 155, 944–954. https://doi.org/10.1017/s0016756816001205.

Pole, M., Wang, Y., Dong, C., Xie, X., Tian, N., Li, L., Zhou, N., Lu, N., Xie, A., Zhang, X.J. P., Palaeoenvironments, 2018. Fires and storms—a Triassic–Jurassic transition section in the Sichuan Basin, China. Palaeobiodiv. Palaeoenviron. 98, 29–47. https://doi.org/10.1007/s12549-017-0315-y.

Price, G.D., 1999. The evidence and implications of polar ice during the Mesozoic. Earth Sci. Rev. 48, 183–210. https://doi.org/10.1016/s0012-8252(99)00048-3.

Price, G., Baker, S., VanDeVelde, J., Clemence, M.-E., 2016. High-Resolution Carbon Cycle and Seawater Temperature Evolution during the Early Jurassic (Sinemurian-Early Pliensbachian). https://doi.org/10.1002/2016GC006541.

Prochnow, S.J., Nordt, L.C., Atchley, S.C., Hudec, M.R., 2006. Multi-proxy paleosol evidence for middle and late Triassic climate trends in eastern Utah. Palaeogeogr. Palaeoclimatol. Palaeoecol. 232, 53–72. https://doi.org/10.1016/j.palaeo.2005.08.011.

Qian, L.J., Shi, Z.Q., Li, Z.W., Ou, L.H., 2010. Fossil wood of the upper triassic xujiahe formation on the western margin of Sichuan Basin:implication for palaeoclimate. Acta Sedimentol. Sin. 28, 324–330 (in Chinese with English Abstract). 10.14027/j.cnki.cjxb.2010.02.004.

Qiu, X., Liu, C., Mao, G., Deng, Y., Wang, F., Wang, J., 2015. Major, trace and platinum-group element geochemistry of the Upper Triassic nonmarine hot shales in the Ordos basin, Central China. Appl. Geochem. 53, 42–52. https://doi.org/10.1016/j.apgeochem.2014.11.028.

Rasmussen, C., Brantley, S., Richter, D.d., Blum, A., Dixon, J., White, A.F., 2011. Strong climate and tectonic control on plagioclase weathering in granitic terrain. Earth Planet. Sci. Lett. 301, 521–530. https://doi.org/10.1016/j.epsl.2010.11.037.

Retallack, G.J., 2005. Pedogenic carbonate proxies for amount and seasonality of precipitation in paleosols. Geology 33, 333–336. https://doi.org/10.1130/g21263.1.

Retallack, G.J., 2009a. Greenhouse crises of the past 300 million years. Geol. Soc. Am. Bull. 121, 1441–1455, 10.1130/b26341.1.

Retallack, G.J., 2009b. Triassic-Jurassic Climates. In: Gornitz, V. (Ed.), Encyclopedia of Paleoclimatology and Ancient Environments. Springer Netherlands, Dordrecht, pp. 962–968.

Retallack, G.J., 2013. Permian and Triassic greenhouse crises. Gondwana Res. 24, 90–103. https://doi.org/10.1016/j.gr.2012.03.003.

Retallack, G.J., Conde, G.D., 2020. Deep time perspective on rising atmospheric CO2. Glob. Planet. Chang. 189 https://doi.org/10.1016/j.gloplacha.2020.103177.

Robinson, S.A., Ruhl, M., Astley, D.L., Naafs, B.D.A., Farnsworth, A.J., Bown, P.R., Jenkyns, H.C., Lunt, D.J., O'Brien, C., Pancost, R.D., Markwick, P.J., Heimhofer, U., 2017. Early Jurassic North Atlantic sea-surface temperatures from TEX86palaeothermometry. Sedimentology 64, 215–230. https://doi.org/10.1111/sed.12321.

Roger, F., Jolivet, M., Malavieille, J., 2010. The tectonic evolution of the Songpan-Garzê (North Tibet) and adjacent areas from Proterozoic to Present: A synthesis. J. Asian Earth Sci. 39, 254–269. https://doi.org/10.1016/j.jseaes.2010.03.008.

Royer, D.L., 2014. Atmospheric CO2 and O2 During the Phanerozoic: Tools, Patterns, and Impacts, Treatise on Geochemistry, pp. 251–267.

Ruebsam, W., Mayer, B., Schwark, L., 2019. Cryosphere carbon dynamics control early Toarcian global warming and sea level evolution. Glob. Planet. Chang. 172, 440–453. https://doi.org/10.1016/j.gloplacha.2018.11.003.

Ruffell, A., Simms, M.J., Wignall, P.B., 2016. The Carnian Humid Episode of the late Triassic: a review. Geol. Mag. 153, 271–284. https://doi.org/10.1017/s0016756815000424.

Scherer, C.M.S., Goldberg, K., 2007. Palaeowind patterns during the latest Jurassic-earliest Cretaceous in Gondwana: evidence from aeolian cross-strata of the Botucatu Formation, Brazil. Palaeogeogr. Palaeoclimatol. Palaeoecol. 250, 89–100. https://doi.org/10.1016/j.palaeo.2007.02.018.

Sellwood, B.W., Valdes, P.J., 2006. Mesozoic climates: general circulation models and the rock record. Sediment. Geol. 190, 269–287. https://doi.org/10.1016/j.sedgeo.2006.05.013.

Sellwood, B.W., Valdes, P.J., 2008. Jurassic climates. Proc. Geol. Assoc. 119, 5–17. https://doi.org/10.1016/s0016-7878(59)80068-7.

Shao, L.Y., Li, Y.J., X, J.F., Gao, C.X., Zhang, C., Liang, W.L., Li, G.M., Chen, Z.S., Peng, Z. Q., Cheng, A.G., 2014. Sequecne Stratigraphy and lithofacies palaography of the Late Triassic Coal Measures in South China. J. Paleogeogr. 16, 613–630 (in Chinese with English Abstract). https://doi.org/10.7605/gdlxb.2014.05.050.

Singer, A., 1980. The paleoclimatic interpretation of clay minerals in soils and weathering profiles. Earth Sci. Rev. 15, 303–326. https://doi.org/10.1016/0012-8252(80)90113-0.

Stefani, M., Furin, S., Gianolla, P., 2010. The changing climate framework and depositional dynamics of Triassic carbonate platforms from the Dolomites. Palaeogeogr. Palaeoclimatol. Palaeoecol. 290, 43–57 https://doi.org/http://202.114.202.219:80/rwt/ELSEVIER/https/MSYXTLUQPJUB/10.1016/j.palaeo.2010.02.018.

Steinthorsdottir, M., Jeram, A.J., McElwain, J.C., 2011. Extremely elevated CO2 concentrations at the Triassic/Jurassic boundary. Palaeogeogr. Palaeoclimatol. Palaeoecol. 308, 418–432. https://doi.org/10.1016/j.palaeo.2011.05.050.

Sun, Y., Joachimski, M.M., Wignall, P.B., Yan, C., Chen, Y., Jiang, H., Wang, L., Lai, X., 2012. Lethally hot temperatures during the early triassic greenhouse. Science 338, 366–370. https://doi.org/10.1126/science.1224126.

Sun, Y.D., Wignall, P.B., Joachimski, M.M., Bond, D.P.G., Grasby, S.E., Lai, X.L., Wang, L. N., Zhang, Z.T., Sun, S., 2016. Climate warming, euxinia and carbon isotope perturbations during the Carnian (Triassic) Crisis in South China. Earth Planet. Sci. Lett. 444, 88–100. https://doi.org/10.1016/j.epsl.2016.03.037.

Taheri, A., Jafarzadeh, M., Armstrong-Altrin, J.S., Mirbagheri, S.R., 2018. Geochemistry of siliciclastic rocks from the Shemshak Group (Upper Triassic-Middle Jurassic), northeastern Alborz, northern Iran: implications for palaeoweathering, provenance, and tectonic setting. Geol. Quart. 62, 522–535. https://doi.org/10.7306/gq.1433.

Taylor, S.R., McClennan, S.M., 1985. The Continental Crust: Its Composition and Evolution. Blackwell, Oxford.

Tian, N., Wang, Y., Philippe, M., Li, L., Xie, X., Jiang, Z., 2016. New record of fossil wood Xenoxylon from the Late Triassic in the Sichuan Basin, southern China and its paleoclimatic implications. Palaeogeogr. Palaeoclimatol. Palaeoecol. 464, 65–75. https://doi.org/10.1016/j.palaeo.2016.02.006.

Tramoy, R., Schnyder, J., Tu, T.T.N., Yans, J., Jacob, J., Sebilo, M., Derenne, S., Philippe, M., Huguet, A., Pons, D., Baudin, F., 2016. The Pliensbachian-Toarcian paleoclimate transition: New insights from organic geochemistry and C, H, N isotopes in a continental section from Central Asia. Palaeogeogr. Palaeoclimatol. Palaeoecol. 461, 310–327. https://doi.org/10.1016/j.palaeo.2016.08.020.

Trotter, J.A., Williams, I.S., Nicora, A., Mazza, M., Rigo, M., 2015. Long-term cycles of Triassic climate change: a new delta O-18 record from conodont apatite. Earth Planet. Sci. Lett. 415, 165–174. https://doi.org/10.1016/j.epsl.2015.01.038.

Wang, Y., 2002. Fern ecological implications from the Lower Jurassic in western Hubei, China. Rev. Palaeobot. Palynol. 119, 125–141. https://doi.org/10.1016/s0034-6667(01)00133-6.

Wang, H., Chu, X., Liu, B., 1985. Atlas of the Paleogeography of China. Cartographic Publishing Hourse, Beijing China, pp. 90–106.

Wang, Y., Fu, B., Xie, X., Huang, Q., Li, K., Li, G., Liu, Z., Yu, J., Pan, Y., Tian, N.J.U.o.S., Technology of China Press, H, 2010. The Terrestrial Triassic and Jurassic Systems in the Sichuan Basin. China. 1-216.

Wang, P., Du, Y., Yu, W., Algeo, T.J., Zhou, Q., Xu, Y., Qi, L., Yuan, L., Pan, W., 2020. The chemical index of alteration (CIA) as a proxy for climate change during glacial-interglacial transitions in Earth history. Earth Sci. Rev. 201, 103032. https://doi.org/10.1016/j.earscirev.2019.103032.

Wierzbowski, H., Bajnai, D., Wacker, U., Rogov, M.A., Fiebig, J., Tesakova, E.M., 2018. Clumped isotope record of salinity variations in the Subboreal Province at the Middle-Late Jurassic transition. Glob. Planet. Chang. 167, 172–189. https://doi.org/10.1016/j.gloplacha.2018.05.014.

Wilson, K., Pollard, D., Hay, W., Thompson, S., Wold, C., 1994. General circulation model simulations of Triassic climates: Preliminary results. Spec. Paper Geol. Soc. Am. 288, 91–116. https://doi.org/10.1130/SPE288-p91.

Wu, H.N., Zhu, R., Courtillot, V., Bai, L., Xing, J., Zhao, Y., Yang, G., 1999. Paleomagnetic results of Paleozoic and Mesozoic rocks from Xingshan-Zigui section in Hubei Province, South China. Sci. China(Series D:Earth Sciences) 42, 182–194 https://doi.org/CNKI:SUN:JDXG.0.1999-02-008.

Xu, Z.J., Cheng, R.H., Zhang, L., Wang, L.L., Kong, Y., 2012. The geochemistry records of sea-level relative movement and paleoclimatic evolution of south CHINA Continiental Margin in Late Triassic-Early-Middle Jurassic. Earth Sci. J. China Univ. Geosci. 37, 113–124 (in Chinese with English Abstract). https://doi.org/10.3799/dqkx.2012.011.

Xu, W., Ruhl, M., Jenkyns, Hugh C., Hesselbo, Stephen P., Riding, James B., Selby, D., Naafs, B., David, A., Weijers, Johan W.H., Pancost, Richard D., Tegelaar, Erik W., Idiz, Erdem F., 2017. Carbon sequestration in an expanded lake system during the Toarcian oceanic anoxic event. Nat. Geosci. 10, 129–134. https://doi.org/10.1038/ngeo2871.

Yang, J., Cawood, P.A., Du, Y., Li, W., Yan, J., 2016. Reconstructing Early Permian tropical climates from chemical weathering indices. Geol. Soc. Am. Bull. 128, 739–751. https://doi.org/10.1130/b31371.1.

Yi, Z., Liu, Y., Meert, J.G., 2019. A true polar wander trigger for the Great Jurassic East Asian Aridification. Geology 47, 1112–1116. https://doi.org/10.1130/g46641.1.

Yokoyama, M., Liu, Y., Otofuji, Y.I., Yang, Z., 1999. New Late Jurassic palaeomagnetic data from the northern Sichuan basin: implications for the deformation of the Yangtze craton. Geophys. J. Int. 139, 795–805. https://doi.org/10.1046/j.1365-246x.1999.00951.x.

Yokoyama, M., Liu, Y., Halim, N., Otofuji, Y.I., 2001. Paleomagnetic study of Upper Jurassic rocks from the Sichuan basin: tectonic aspects for the collision between the Yangtze Block and the North China Block. Earth Planet. Sci. Lett. 193, 273–285. https://doi.org/10.1016/s0012-821x(01)00498-8.

Zeng, Z., Zhu, H., Yang, X., Zeng, H., Hu, X., Xia, C., 2019. The pangaea megamonsoon records: evidence from the Triassic Mungaroo Formation, Northwest Shelf of Australia. Gondwana Res. 69, 1–24. https://doi.org/10.1016/j.gr.2018.11.015.

Zhang, Z.L., Meng, F.S., 1987. Biostratigraphy of the Yangtze Gorge Area (4): Triassic and Jurassic. Geological Publishing House, Beijing, pp. 1–487.

Zhao, Z., Zhao, J., Wang, H., Liao, J., Liu, C., 2007. Distribution characteristics and applications of trace elements in Junggar Basin. Nat. Gas Explor. 30, 30–33 (in Chinese with English Abstract).

Zhao, J., Dong, Y., Huang, B., 2020. Paleomagnetic constraints of the lower triassic strata in South Qinling Belt: Evidence for a discrete terrane between the North and South China Blocks. Tectonics 39. https://doi.org/10.1029/2019tc005698.

Zhou, N., Wang, Y., Ya, L., Porter, A.S., Kürschner, W.M., Li, L., Lu, N., McElwain, J.C., 2020. An inter-comparison study of three stomatal-proxy methods for CO2 reconstruction applied to early Jurassic Ginkgoales plants. Palaeogeogr. Palaeoclimatol. Palaeoecol. 542, 109547. https://doi.org/10.1016/j.palaeo.2019.109547.